Research Square

Preprints are preliminary reports that have not undergone peer review.
They should not be considered conclusive, used to inform clinical practice,
or referenced by the media as validated information.

An untethered sub-gram flapping-wing flight system achieves sustained self-stabilizing and controllable flight

Dingbang Xiao

dingbangxiao@nudt.edu.cn

National University of Defense Technology College of Intelligent Science and Technology
https://orcid.org/0000-0002-1591-7220

Xiang Lu
National University of Defense Technology College of Intelligent Science and Technology

Jie Chen
National University of Defense Technology College of Intelligent Science and Technology

Yulie Wu
National University of Defense Technology

Yang Chen
National University of Defense Technology College of Intelligent Science and Technology

Canhui Yin
National University of Defense Technology College of Intelligent Science and Technology

Zixin Deng
National University of Defense Technology College of Intelligent Science and Technology

Chunyan Qu
National University of Defense Technology College of Intelligent Science and Technology

Kun Lu
National University of Defense Technology College of Intelligent Science and Technology

Xuezhong Wu
National University of Defense Technology

Physical Sciences - Article

Keywords:

Posted Date: February 9th, 2026

DOI: https://doi.org/10.21203/rs.3.rs-8253091/v1

License: This work is licensed under a Creative Commons Attribution 4.0 International License.
Read Full License

Additional Declarations: There is **NO** Competing Interest.

An untethered sub-gram flapping-wing flight system achieves sustained self-stabilizing and controllable flight

Xiang Lu[1,3], Jie Chen[1,3], Yulie Wu[1,2] ✉, Yang Chen[1], Canhui Yin[1,2], Zixin Deng[1,2], Yanchun Qu[1,2], Kun Lu[1,2], Xuezhong Wu[1,2], Dingbang Xiao[1,2] ✉

[1] College of Intelligence Science and Technology, National University of Defense Technology; Changsha 410073, China.

[2] National Key Laboratory of Equipment State Sensing and Smart Support, National University of Defense Technology; Changsha 410073, China.

✉Corresponding author. Email: dingbangxiao@nudt.edu.cn, ylwu@nudt.edu.cn.

[3]These authors contributed equally to this work.

Abstract: Insect-scale flapping-wing micro aerial vehicles (FWMAVs) offer great potential for applications like search and rescue, but face severe power and payload constraints at sub-gram scales, precluding sustained untethered flight. This study presents a cross-shaped four-piezoelectric-drive V-wing micro aerial vehicle (FVW-Fly), weighing 389 mg with a 6.8 cm wingspan, which achieves a lift-to-weight ratio of 4.75. Waveform modulation boosts the driving efficiency of a 173 mg circuit to 45%, while mechanical self-stabilization enhances flight stability. Integrated with a 350 mg battery, the 984 mg system achieves the first untethered, sustained, stable flight for a sub-gram FWMAV. Its maximum flight altitude exceeds 10 meters, and the low-power single-cycle continuous flight time exceeds 240 seconds, demonstrating untethered controlled altitude and disturbance resilience flight, marking a groundbreaking milestone.

Inspired by the remarkable flight efficiency and maneuverability of insects, insect-scale flapping-wing micro air vehicles (FWMAVs)[1] have emerged as a frontier research topic in microrobot, holding significant potential for operations in confined spaces—such as post-disaster search and rescue, infrastructure inspection, environmental monitoring, and swarm coordination[2] . However, scaling conventional motor-driven transmissions[3–6] to sub-gram insect dimensions is fundamentally limited by frictional losses and reduced lift-to-power ratios. Consequently, novel actuation strategies, including piezoelectric actuators[7–10], dielectric elastomer actuators (DEAs)[11,12], and electromagnetic systems[13–15], have been explored to develop efficient insect-scale flapping propulsion. However, limited payload capacity and low power-conversion efficiency typically necessitate tethering to external power sources[16,17] and control systems[18,19], precluding autonomous flight in practical scenarios.

Recent efforts toward untethered insect-scale FWMAVs focus on enhancing payload capacity, optimizing flight control and passive stability, and miniaturizing power electronics. Piezoelectric systems (e.g., RoboBee [16,20–27]) achieved brief untethered flight under high-intensity lighting via aerodynamic optimization and circuit miniaturization[27], while adaptive control enabled short tethered hovering[28–30]. Incorporating aerodynamic dampers further provided 1–2 s of open-loop altitude stability[31,32], simplifying control requirements. RoboFly demonstrated the first wireless liftoff (<0.1 s) via laser power delivery to an ultra-light piezoelectric circuit[9,33]. Utilized high-efficiency PIN-PMN-PT piezoelectric crystals[34] and a twin-wing design[35], with a miniaturized boost converter enabled brief untethered flight (<1 s) using either radiofrequency[36] or battery power[37]. A robust DEA-based FWMAV[11] using a spherical four-bar linkage, increasing peak lift from 1.8 mN to 6.45 mN via multilayer fabrication and electrode optimization[38], enabled complex maneuvers with external tracking[39–41]. Critically, however, no insect-scale (sub-gram) FWMAV achieves sustained, stable untethered flight. Current untethered systems rely on ground-based power (lasers/RF), lack closed-loop control (collapsing within 1 s), and exhibit insufficient endurance due to payload constraints and inefficient power electronics. Mature lithium batteries[42–44] thus remain an unrealized solution for autonomous operation.

Here, we present a 389 mg a cross-shaped four-piezoelectric-drive V-wing micro aerial vehicle (FVW-Fly) (6.8 cm wingspan). Its tuning-fork-inspired omnidirectional flapping motion enhances aerodynamic efficiency by 27.5%, the maximum lift is 2.55 times that of the linear dual-drive structure[17], yielding a maximum lift-to-

weight ratio of 4.75. Combined with an optimized passive stabilization mechanism, the vehicle exhibits exceptional self-stabilized and disturbance rejection. We further developed a lightweight and high-efficiency high-voltage drive control electronic system (HVDCE) (173 mg; 45% efficiency) with Bluetooth communication and time of flight (TOF) sensing, enabling low-distortion sinusoidal output and flight altitude perception. Leveraging this self-stabilizing FVW-Fly platform and the HVDCE, we integrated an ultralight lithium battery to construct a fully integrated, sub-gram-scale untethered FVW-Fly system. The complete system has a wingspan of 6.8 cm and a total mass of 984 mg. Powered solely by its onboard battery, the system successfully demonstrated controlled altitude flight, stable hovering at designated heights, and recovery flight following disturbances. Experimental validation confirmed that this sub-gram-scale untethered FVW-Fly system achieves a maximum ascent altitude exceeding 10 m and a single-flight endurance of 240 s, rapidly recovering stable flight attitude after deliberate disturbances. Critically, this work represents the first reported sub-gram-scale untethered FWMAV system, controlled continue flight.

Structure design of FVW-Fly with high lift capacity

To achieve high payload capacity and self-stabilization capabilities at insect scale, We present a 389 mg, 6.8 cm wingspan flapping-wing micro aerial vehicle (FWMAV) with superior payload capacity and passive stabilization, enabled by four orthogonally arranged piezoelectric direct-drive modules in a cross configuration (Fig. 1, A and B). Each module comprises a Y-shaped bimorph actuator, two passively torsional wings, and an alignment slot, generating lift via direct-drive flapping and passive pitching (Extended Data Fig. 1, Movie S1). A circumferentially symmetric self-stabilization mechanism is vertically integrated above the fuselage (Fig. 1C).

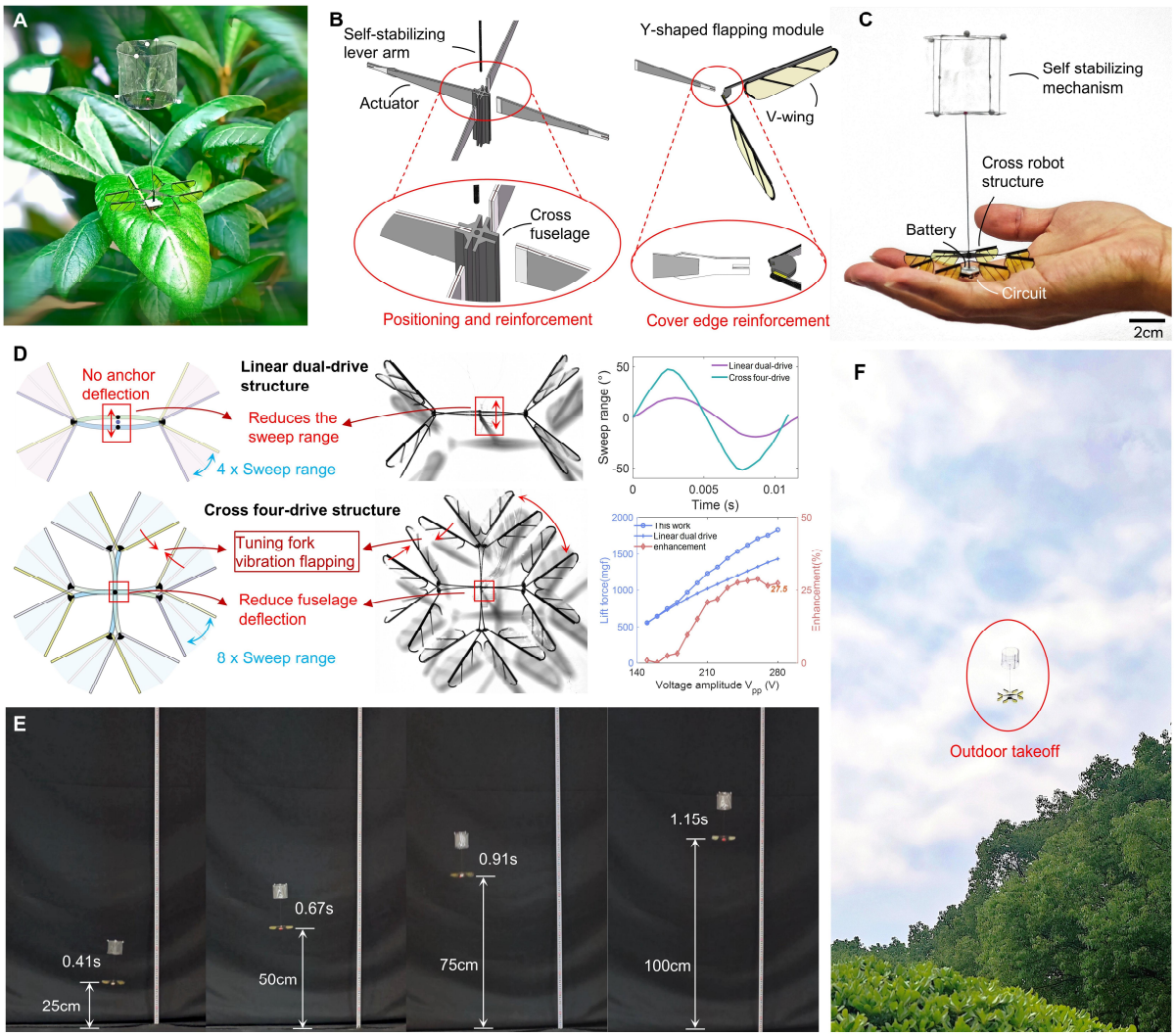


Fig. 1. A sub-gram FWMAV enabling sustainable untethered and self-stabilized flight. (A) The robot perched on a leaf. **(B)** Reinforced design of the pluggable cross-embedded fuselage and piezoelectric actuator section with edge wrapping, enhancing operational longevity. **(C)** The main component of the untethered FVW-Fly system. **(D)** Tuning-fork vibration flapping reduces fuselage and motion coupling between actuators during flight, resulting in a 2.55-fold increase in maximum lift compared to linear dual-drive configurations. **(E)** An untethered FVW-Fly system ascending to different altitudes. **(F)** The untethered FVW-Fly system during outdoor takeoff.

Optimization of self-stabilizing mechanism

To endow the robot with intrinsic self-stabilization and disturbance rejection capabilities, we previously introduced a circumferential symmetry-based self-stabilizing mechanism[17]. Compared to our prior work, the FVW-Fly utilizes a full-periphery flapping wing configuration. This enhances aerodynamic efficiency but also increases the inherent unbalanced torque. Additionally, the integrated drive circuitry and battery module significantly shift the system's center of gravity. Consequently, the previous stabilizing mechanism proves insufficient for maintaining stable autonomous flight (Extended Data Fig.3).

The stabilizing effect primarily arises from the restoring torque generated by the damping cylinder. The magnitude of this restoring torque depends on the damping cylinder's effective area and its moment arm. To modify the restoring torque without increasing cylinder mass, we adjusted the length of the moment arm. Simulation analysis identified an optimal strut length of 55 mm (Extended Data Fig.3C, Extended Data Table 1). However, accounting for practical system asymmetries and initial torque discrepancies in the physical prototype, a slightly longer strut length of 70 mm was implemented. Experimental validation confirmed that this parameter yields better self-stabilizing performance in the untethered FVW-Fly system.

External drive characterization of the FVW-Fly

Static constraint tests were performed on the robot to evaluate its performance. The measured frequency response characteristics of the flapping module revealed a resonant frequency of 88 Hz. Under the maximum drive signal (280 V, 88 Hz), the output characteristics of the flapping angle and pitch angle were measured (Fig. 2, A and B). The maximum flapping angle reached 13.3° (Fig. 2C), representing a 34.3% increase compared to prior designs[17]. This enhancement is advantageous for lift generation. The pitch angle range was reduced to -55° to 45° (Fig. 2C), primarily to prevent wing interference during flapping. Twice lift frequency sweep tests were performed on the flapping module using varying drive amplitudes (140 V, 160 V, 180 V, 200 V) (Fig. 2E). The results demonstrate that lift output peaks at 88 Hz, corresponding to the resonant frequency of the flapping module. All subsequent flight experiments utilized this fixed frequency. To characterize the relationship between lift and drive amplitude, amplitude sweep tests were conducted at the fixed frequency of 88 Hz (Fig. 2F). The robot achieved a maximum lift force of 1850 mg and a maximum lift-to-weight ratio of 4.75 (Fig. 2H), representing one of the highest ratios reported for FWMAV and demonstrating sufficient payload capacity for tether-free operation.

Open-loop self-stabilized takeoff tests were performed on the FVW-Fly equipped with a self-stabilization mechanism. The takeoff velocity under varying external drive signal amplitudes was measured (Fig. 2G). The average takeoff velocity, recorded using a high-speed motion capture system (Fig. 2G, Extended Data Fig.4, movie S3), maximum average takeoff velocity exceeded 1.6 m/s. This performance ranks among the highest stable takeoff speeds reported for insect-scale FWMAVs (Fig. 2H).

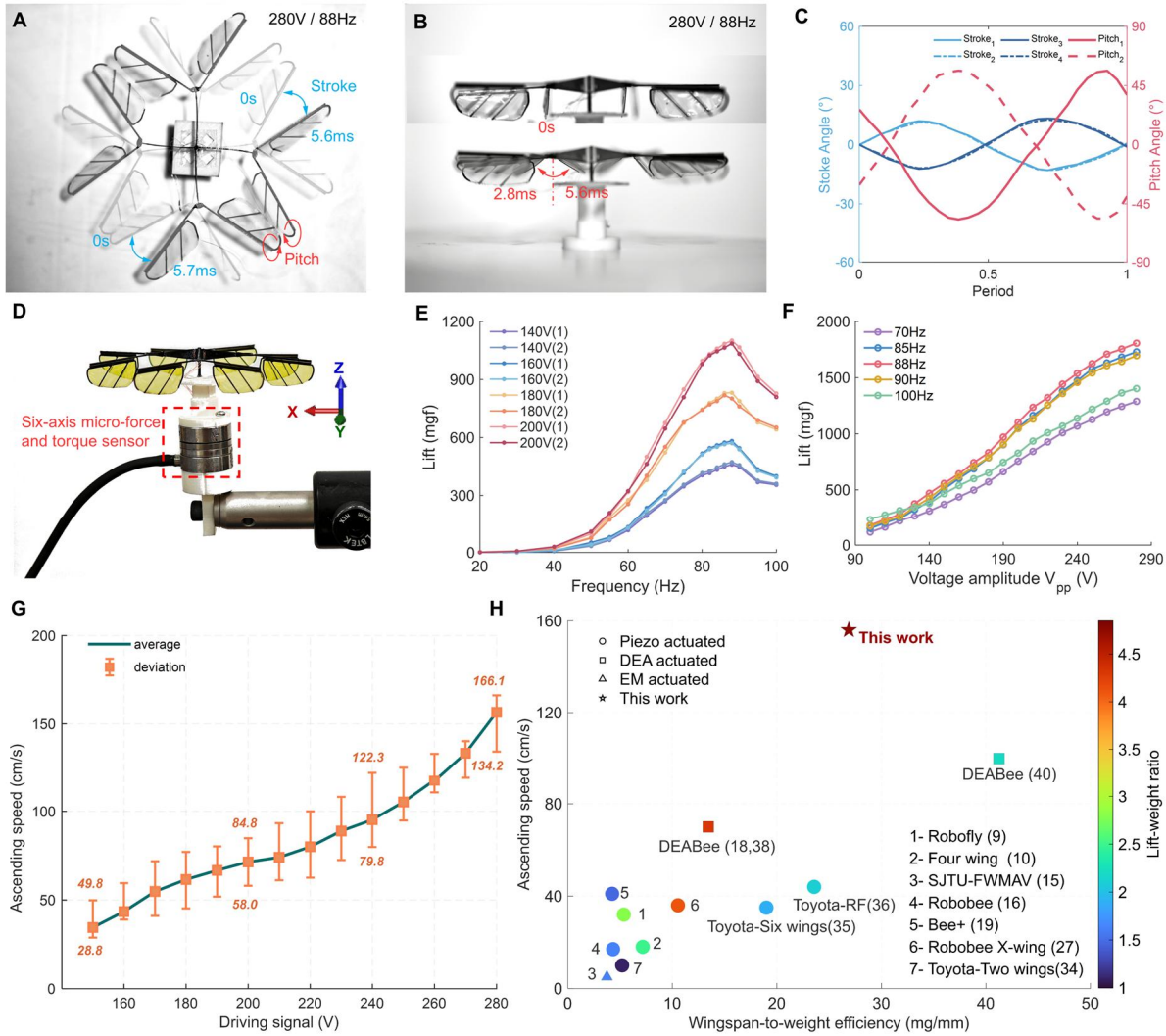


Fig. 2. Static properties and external drive takeoff velocity characterization of the FVW-Fly. (A and B) Composite diagram illustrating the flapping stroke motion and passive pitching motion of the robot under 280 V and 88 Hz excitation. **(C)** The test fitting curves of the flapping wing travel angle and pitch angle corresponding to panels (A) and (B). **(D)** Static mechanical property testing of the robot using a six-axis micro-force test platform. **(E)** The frequency response characteristics of the robot's lift force show an optimal driving frequency of 88Hz. **(F)** The amplitude response characteristics of the robot lift force, achieving a maximum lift-to-weight ratio of 4.75. **(G)** Takeoff velocity of the robot under varying amplitudes of the external drive signal, reaching a maximum velocity exceeding 1.6 m/s. **(H)** The performance metrics for representative externally driven insect-scale flapping-wing micro air vehicles: takeoff velocity, wing loading ratio, and lift-to-weight ratio.

Design of high-voltage drive control electronic system

Achieving untethered flight in sub-gram FWMAVs like the FVW-Fly demands ultra-lightweight, high-efficiency power electronics. To actuate its piezoelectric wings, we developed a milligram-scale High-Voltage Drive Control Electronic system (HVDCE) (Fig. 3A). This system, powered by a rechargeable micro lithium-ion battery (3.7 V/10 mAh), receives Bluetooth commands, generates control signals, boosts the low-voltage DC to high voltage, and synthesizes a tailored high-voltage sinusoidal AC drive signal for efficient, low-damage piezoelectric actuation (Fig. 3, B and C).

The HVDCE integrates a microcontroller (MCU) for command processing and signal generation, a time-of-flight (TOF) sensor for altitude perception (Fig. 3D), and a boost inverter for power conversion. Fabricated using double-layer flexible printed circuit (FPC) technology (9 mm x 10 mm, 173 mg total weight), it employs discrete

components and a custom coupled inductor (Fig. 3A). The boost inverter combines a flyback converter for voltage step-up (Step-up ratio: 86) and an H-bridge for inversion, generating the required 210 V, 88 Hz sinusoidal AC signal from the battery.

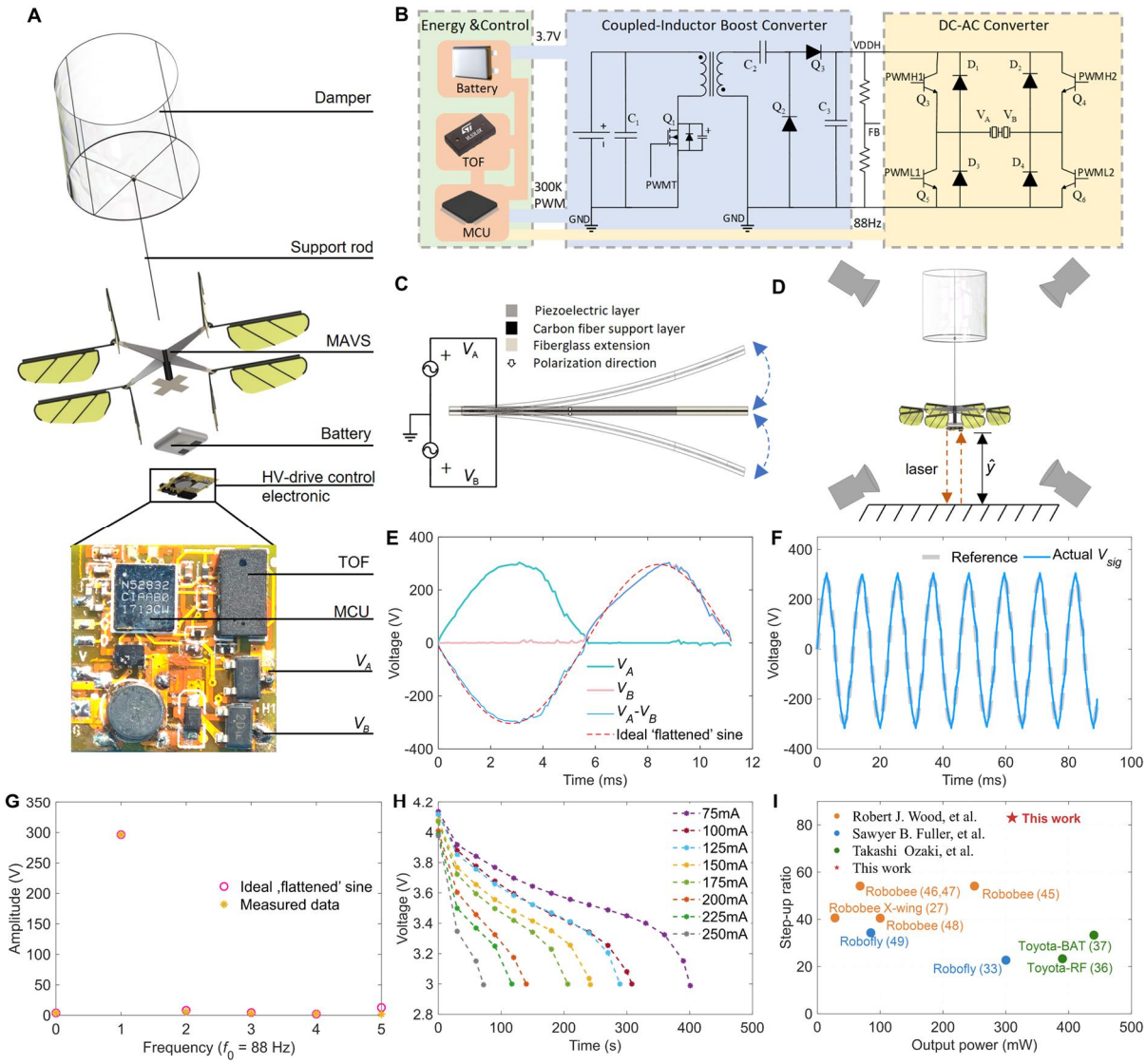


Fig. 3. High-Voltage Drive and Control Electronic System (HVDCE). (A) Exploded view of the overall architecture layout of the untethered micro air vehicle (FVW-Fly): the HVDCE and battery are mounted at the bottom of the vehicle, with the TOF sensor facing downward. **(B)** Schematic block diagram of the HVDCE. **(C)** The piezoelectric actuator consists of upper and lower piezoelectric ceramic plates and a carbon fiber support layer, adopting an alternating drive mode. The high-voltage signals on the upper and lower poles have a phase difference of 180°, and the middle layer is configured with a floating ground. **(D)** During the vehicle's flight, the downward-facing TOF sensor emits infrared laser to achieve altitude measurement. **(E)** Detailed waveforms of the high-voltage signals applied to the two poles of the piezoelectric actuator and their voltage difference when the boost inverter is under load. **(F)** Comparison between the high-voltage AC sinusoidal signal output by the boost inverter and the ideal sinusoidal reference signal (Vpp = 300 V, f = 85 Hz), showing basic overlap. **(G)** Comparison of harmonic components between the high-voltage AC sinusoidal signal output by the inverter and the ideal sinusoidal signal: the fundamental harmonic components basically coincide, while the higher harmonic components are nearly zero. **(H)** Voltage-time curves of

the micro lithium-ion battery under different discharge currents. **(I)** The proposed boost inverter exhibits significant advantages in voltage gain and maximum output power compared to other representative related works.

Key innovations ensure efficiency and actuator longevity:

- Sinusoidal drive: comparing with square waves, it minimizes high-frequency excitation, reducing actuator damage and improving efficiency compared to conventional drives (Fig. 3, E and F).
- Alternating drive scheme: the dual-crystal piezoelectric actuator design eliminates the need for a constant bias voltage. Dynamically adjusting the boost converter output to match the drive signal lowers transformer power consumption (Fig. 3C).
- Shared drive signals: all four piezoelectric actuators utilize a single set of drive signals, significantly reducing circuit weight and complexity.

Performance testing confirms the system's capability. The boost inverter achieves ~45% efficiency driving the FVW-Fly at minimum takeoff power (~400 mW, 100-125 mA current) (Fig. 3I). The micro battery supports over 280 seconds of untethered flight (Fig. 3H). At the actuator's resonant frequency, the inverter delivers >310 mW output power with a maximum voltage exceeding 320 V (Fig. 3G). Harmonic analysis of the 300 V AC output reveals excellent signal fidelity (Total Harmonic Distortion = 6.8%), confirming low-damage, high-efficiency operation.

Compared to existing piezoelectric drive circuits, this boost inverter offers superior voltage gain, higher output power capability (>310 mW), and achieves high energy efficiency at >200 V AC output. Its ultra-lightweight design and minimal component count uniquely meet the stringent power density and load capacity constraints essential for untethered sub-gram FVW-Fly flight.

Design of a sub-gram untethered FVW-Fly system

To achieve untethered flight, based on the FVW-Fly flapping structure, a self-stabilizing mechanism, and a high-voltage drive circuit we proposed, we designed a sub-gram FVW-Fly untethered system (Fig. 1C). While the drive circuit and battery are compact, their combined mass constitutes approximately 3/5 of the total system weight. To mitigate the destabilizing effects of structural asymmetry introduced by this power module, we developed a design strategy for sustained stable hovering (Fig. 3A). This approach involves two key steps:

- Centralized mass placement: the circuit and battery are co-located near the drive center with centrosymmetric mass distribution. This minimizes their moment arm, reducing destabilizing torque.
- Extended stabilizing arm: optimizing the distance between the passive stabilizer and the center of mass lengthens its moment arm. This ensures sufficient restoring torque counters both the inherent vehicle imbalance and torque induced by the power module.

Untethered Flight Performance

For untethered flight operations, the driving signal was remotely regulated via Bluetooth. Initial flight commenced at a relatively low voltage (210 V) to extend battery life and enhance vehicle longevity, ensuring experimental repeatability. At 210 V driving output, the designed drive circuit consumed 400 mW. The robot generated a lift force of 1250 mg, sufficient to lift the entire untethered system and enable stable, sustained vertical ascent (Fig. 1, E and F).

Flight endurance is a critical metric and significant challenge for insect-scale FWMAV transitioning to practical applications. Under remote command, the circuit module delivered a driving signal (210 V, 88 Hz). The system overcame its weight to achieve vertical takeoff, ascended to a position near the ceiling, maintained stable hovering (Fig. 4, A and B). Limited by battery capacity and performance, the untethered FVW-Fly system achieved a maximum single-flight duration of 240 s (movie S4).

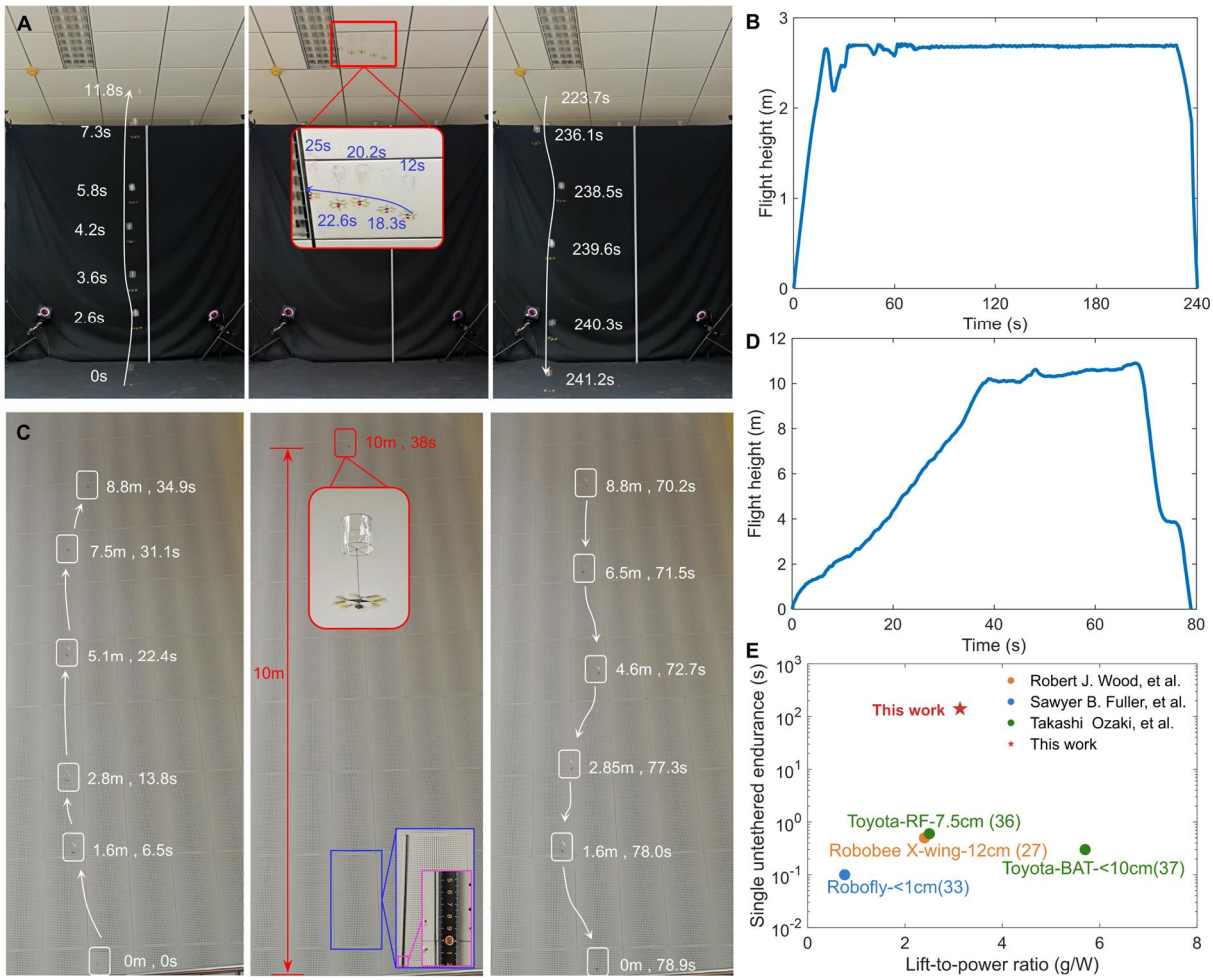


Fig. 4. Flight performance of the sub-gram untethered FVW-Fly system. (A and B) Sustained flight under a 210 V/88 Hz drive signal, **(A)** Composite image of the flight process, and **(B)** Fitted curve of flight altitude versus time. Due to ceiling constraints, the robot maintained a near-constant altitude after reaching the ceiling until landing. **(C and D)** Altitude performance during ascent. **(C)** Composite image of the untethered ascent and descent process. **(D)** Fitted curve of flight altitude versus time corresponding to panels (C), the vehicle achieved a maximum altitude of 10 m. **(E)** Representative examples of sustained flight duration and lift-to-power ratio for untethered insect-scale FWMAVs.

The maximum achievable flight altitude defines the vertical operational range and determines the extreme mission positions accessible to the robot. We conducted ascent tests with the untethered FVW-Fly system. Following the drive input, the vehicle ascended vertically, reaching a maximum altitude exceeding 10 m . It undergoes a small range of offset oscillation flight and then descends slowly (Fig. 4, C and D, movie S5). This maximum ascent height and single-flight duration surpass that of existing sub-gram untethered FWMAVs by over two orders of magnitude (Fig. 4E).

First controlled altitude flight

The ability to hover stably at varying altitudes is a fundamental requirement for practical applications of micro-aerial vehicle (MAV) systems. To address this, we demonstrate, for the first time, highly stable altitude control and sustained hovering flight in a sub-gram untethered FWMAV system. The designed HVDCE integrates a ToF sensor (Fig.3, A and B) mounted on the robto's underside to measure altitude. This enables closed-loop altitude feedback control. The calibrated ToF sensor achieves a resolution of 1 mm and a maximum range of 2 m (Extended Data Fig.5). The ToF sensor continuously feeds back altitude data at 100 Hz. Control

signals, updated at 50 Hz, dynamically adjust the voltage amplitude to stabilize the robot in a controlled hover at the target altitude.

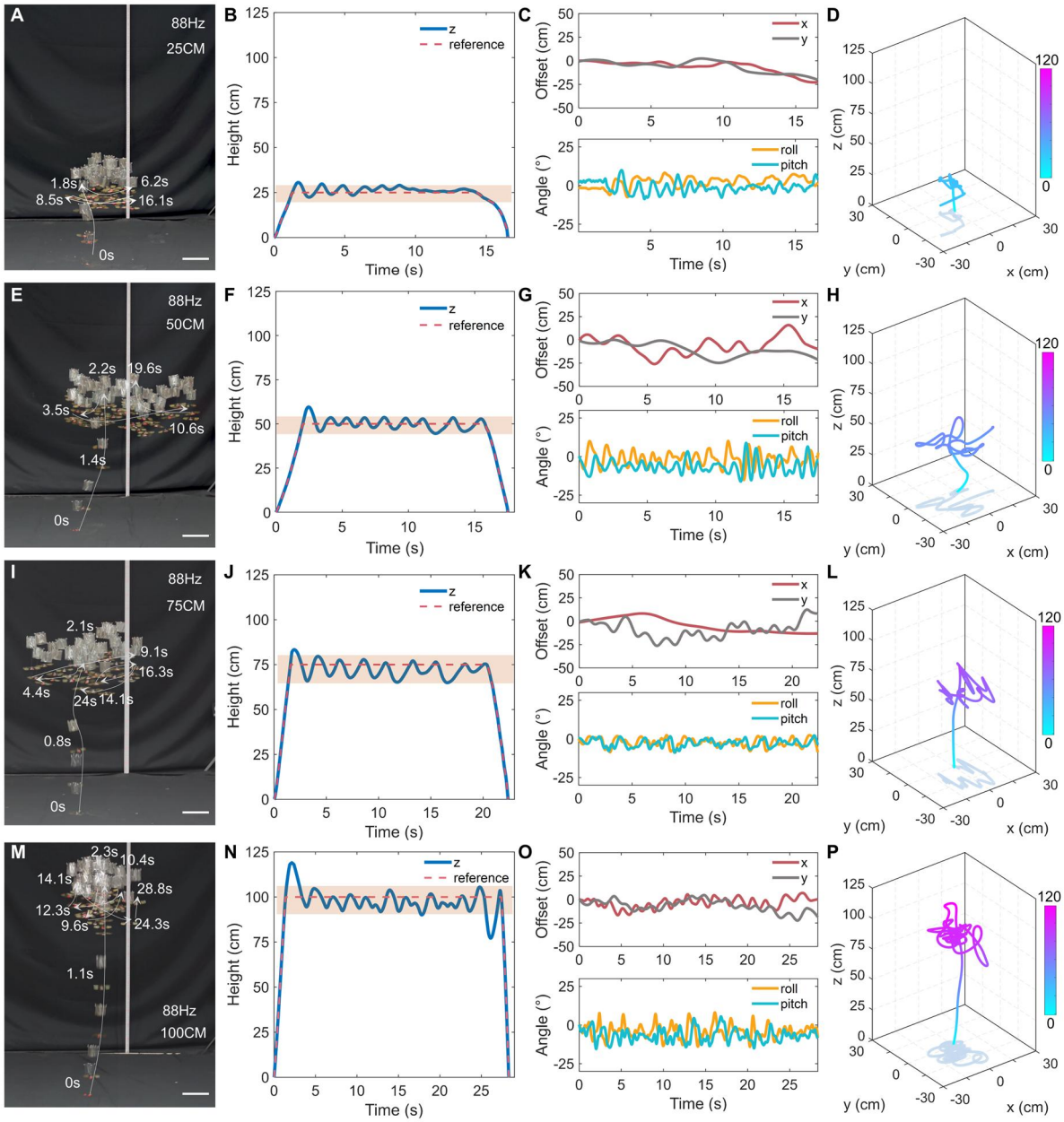


Fig. 5. Flight performance of a sub-gram untethered FVW-Fly system under controlled altitude. (A to D) Fixed altitude flight performance of the robot at a control height of 25 cm. **(E to H)** Fixed altitude flight performance of the robot at a control height of 50 cm. **(I to L)** Fixed altitude flight performance of the robot at a control height of 75 cm. **(M to P)** Fixed altitude flight performance of the robot at a control height of 100 cm. **(B, F, J, and N)** Flight altitude versus time at control heights of 25 cm, 50 cm, 75 cm, and 100 cm, respectively. **(C, G, K, and O)** Horizontal displacement, pitch angle, and roll angle versus time at control heights of 25 cm, 50 cm, 75 cm, and 100 cm, respectively. **(D, H, L, and P)** Trajectory tracking at control heights of 25 cm, 50 cm, 75 cm, and 100 cm, respectively. The color bar indicates the robot's distance from the initial origin point. In this experiment, the position setpoint relative to the motion capture system origin was (0, 0, 0) cm, the pitch and roll setpoints were both 0°.

To characterize the altitude hovering capability of the designed sub-gram untethered FVW-Fly system, we performed a series of controlled hovering experiments at different target heights. The untethered system's pose information was captured with a high-speed motion capture system (Luster, FZMotion, Swift 120A).

Four consecutive flight tests were conducted with the same untethered FVW-Fly system at distinct target altitudes: 25 cm, 50 cm, 75 cm, and 100 cm (Movie S6). Upon receiving the command, the robot rapidly ascended to the vicinity of the target altitude. After a brief oscillatory adjustment period lasting a few seconds, the robot stabilized into a sustained hover near the setpoint. This gradient validated the untethered system 's altitude holding capability across its operational range. According to the experimental results, we presented as composite figures for each altitude (Fig.5, A, E, I and M), alongside plots of altitude variation (Fig.5, B, F, J and N), horizontal position deviation and pitch/roll angle variation (Fig.5, C, G, K and O), and 3D trajectory fitting (Fig.5, D, H, L and P). Experimental results indicate that the untethered FVW-Fly system maintains altitude positioning errors consistently within 10% of the target height across all tested levels. This validates the designed sub-gram untethered flight system's robust flight endurance and repeatable altitude holding performance.

Disturbance-rejection self-stabilizing flight demonstration

The untethered FVW-Fly robot employs a self-stabilizing mechanism generating restorative torque upon deflection, enabling autonomous recovery to vertical orientation. This inherent stability provides significant disturbance rejection, allowing rapid flight recovery post-perturbation. We evaluated this capability through controlled collision and wind gust tests (Movie S7).

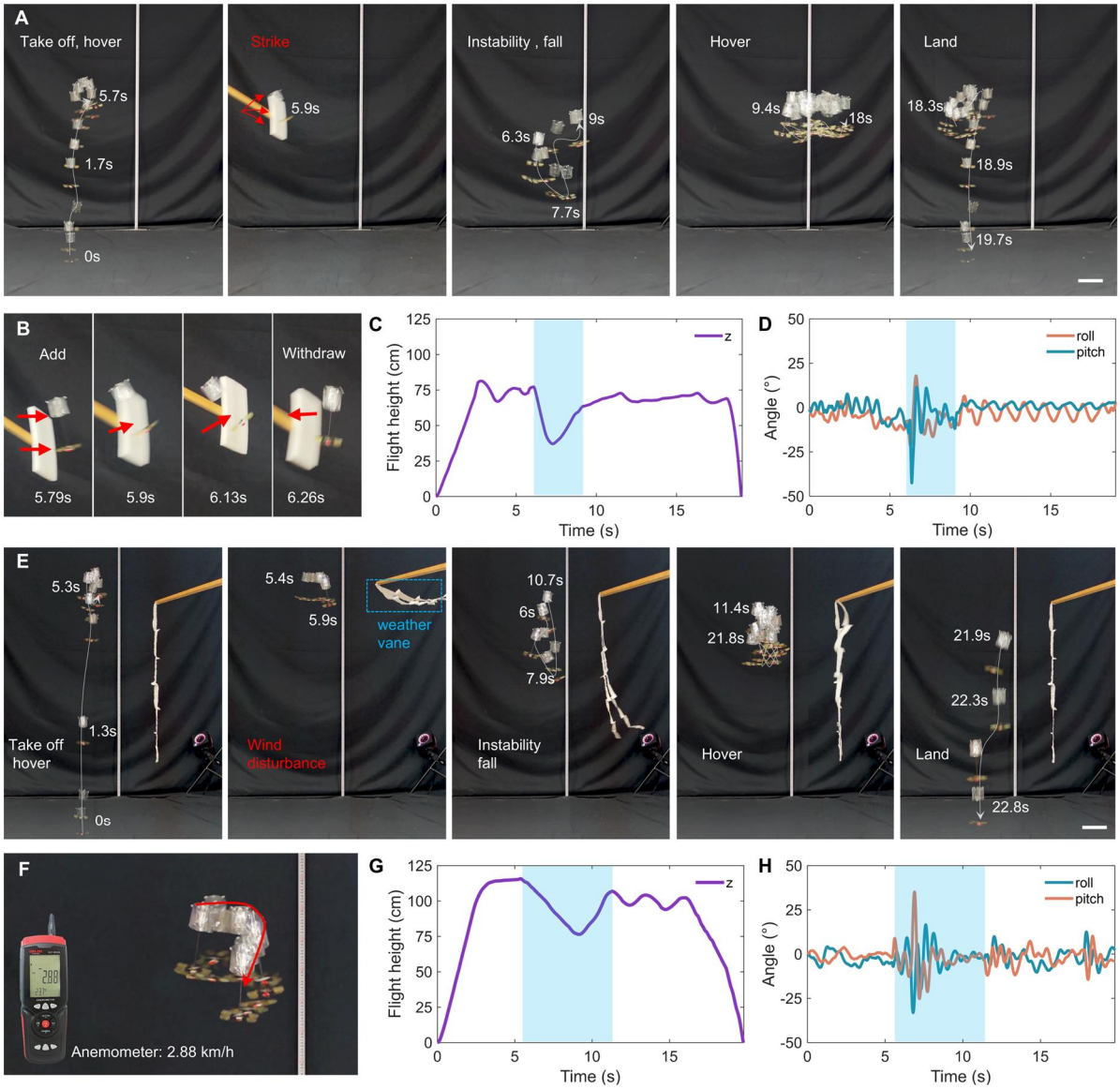


Fig. 6. Disturbance-rejection and self-stabilization flight performance of the sub-gram untethered FVW-Fly system. (A to D) Flight performance under collision disturbance at 75 cm altitude, composite image sequence of flight during collision disturbance (A), close-up detail of the collision event, contact and collision are carried out on the wings and self-stabilizing mechanisms (B), temporal evolution of flight altitude during collision disturbance (C), temporal evolution of the robot's pitch and roll angles during collision disturbance (D). (E to H) Flight performance under gust disturbance at 100 cm altitude, composite image sequence of flight during gust disturbance (E), maximum wind speed test condition (2.88 km/h) (F), temporal evolution of flight altitude during gust disturbance (G), temporal evolution of the untethered system's pitch and roll angles during gust disturbance (H).

Collision rejection: During stable hover (~75 cm altitude), collision disturbances were simulated using a flat plate. Impacts targeted either the wings or the stabilizing mechanism itself (Fig.6, A and B), causing significant instability and oscillations (altitude deviations >40 cm, attitude deflections >45°; Fig. 6C-D). Upon disturbance removal, the system recovered to stable operational bounds within 1.5 s, enabling stable hover near the target altitude, confirming good collision rejection performance.

Wind gust rejection: Wind disturbance rejection is a critical performance requirement for a flight system. To assess wind resistance, lateral gusts were applied during hover using a characterized fan (Fig. 6F). Gusts caused lateral drift, instability, and descent. Post-gust, the system autonomously recovered stability and altitude within seconds (Fig. 6E). Analysis revealed altitude deviations exceeding 35 cm and attitude angle changes >±30° during the gust (Fig. 6G,H). The system consistently returned to stable operation within 3 seconds. This represents the first sub-gram-scale untethered flapping-wing micro air vehicle (FWMAV) capable of such disturbance recovery and sustained flight.

Discussion and Conclusions

This paper proposes a systematic design framework of "Topology optimization to improve lift - Waveform modulation to improve drive circuit efficiency - High multiplier lightweight lithium battery energy supply - Aerodynamic damping mechanism to achieve stabilizing and interference immunity- Active position control to achieve high controllability", which provides innovative solutions to key technical problems of FWMAV piloting without cables. Through system-level integrated design, we successfully developed an untethered, sub-gram-scale FWMAV capable of autonomous flight control. The resulting system integrates a four-piezoelectric-element omnidirectional propulsion unit, an aerodynamic self-stabilization mechanism, a milligram-scale ultra-lightweight high-voltage drive circuit, and an ultra-lightweight lithium battery. With a wingspan of 6.8 cm and a total mass of 984 mg, it achieves self-stabilized, altitude-controllable flight.

Experimental validation confirms stable take-off at a minimum drive voltage of 210 V and flight power consumption of 400 mW. Under optimal driving conditions (280 V, 88 Hz), the robot generates a peak lift force of 1850 mg, yielding a lift-to-weight ratio of 4.75—the highest reported for insect-scale untethered FWMAVs. The system achieves a maximum flight altitude exceeding 10 meters and a continuous flight duration of over 240 seconds, surpassing existing sub-gram untethered FWMAVs by two orders of magnitude in both metrics. Critically, it demonstrated controllable constant-altitude flight within a 2-meter range and inherent stability against collisions, gusts, and multiple strikes. It represents the first sub-gram-scale untethered FWMAV to achieve sustained, controllable, and disturbance-resistant flight, marking a significant milestone in the development of sub-gram-scale untethered FWMAVs. This work provides a novel technological pathway for achieving autonomous, controllable flight in FWMAVs and establishes a crucial technical foundation for their practical deployment in real-world scenarios such as disaster response and environmental monitoring.

The limited heat dissipation and constrained continuous discharge capacity of the current micro lithium battery hinder the sustained flight duration of the system. The integration degree of the drive control circuit and the battery module is relatively low, occupying a considerable load of the system. To further enhance MAV flight performance, future efforts will focus on the following key areas: (1) Increase the energy density and capacity of the battery, and combine the charging and power supply of photovoltaic cells to provide a solution for the long-time flight of the untethered flight system; (2) Expand the integration of the circuit system's functions with the untethered flight system, carry out chip-based design of the drive control circuit module, reduce the weight of the drive control module, provide load space for functional loads, and thereby further promote the practical application of the FWMAV system.

References

1. R. J. Wood, B. Finio, J. P. Whitney et al., Progress on 'pico' air vehicles. Int. J. Robot. Res. 31, 1292–1302 (2012).
2. H. V. Phan, H. C. Park, Insect-inspired, tailless, hover-capable flapping-wing robots: Recent progress, challenges, and future directions. Prog. Aerosp. Sci. 111, 100573 (2019).
3. M. Karásek et al., A tailless aerial robotic flapper reveals that flies use torque coupling in rapid banked turns. Science 361, 1089–1094 (2018).
4. Z. Tu, F. Fei, X. Deng, Untethered flight of an at-scale dual-motor hummingbird robot with bio-inspired decoupled wings. IEEE Robot. Autom. Lett. 5, 4194–4201 (2020).
5. H. V. Phan, H. C. Park, Mechanisms of collision recovery in flying beetles and flapping-wing robots. Science 370, 1214–1219 (2020).
6. H. V. Phan, H. C. Park, D. Floreano, Passive wing deployment and retraction in beetles and flapping microrobots. Nature 632, 1067–1072 (2024).
7. R. J. Wood, The first takeoff of a biologically inspired at-scale robotic insect. IEEE Trans. Robot. 24, 341–347 (2008).
8. X. Lu et al., A high liftoff speed insect-scale aerial robot direct-driven with piezoelectric bimorph PZT actuator. *Chin. J. Aeronaut*. 38, 181–193 (2025).
9. Y. M. Chukewad, J. James, A. Singh, S. Fuller, RoboFly: An insect-sized robot with simplified fabrication that is capable of flight, ground, and water surface locomotion. IEEE Trans. Robot. 37, 2025–2040 (2021).
10. S. B. Fuller, Four wings: An insect-sized aerial robot with steering ability and payload capacity for autonomy. IEEE Robot. Autom. Lett. 4, 570–577 (2019).
11. Y. Chen et al., Controlled flight of a microrobot powered by soft artificial muscles. Nature 575, 324–329 (2019).
12. S. Kim et al., Laser-assisted failure recovery for dielectric elastomer actuators in aerial robots. Sci. Robot. 8, eadf4278 (2023).
13. Z. Liu et al., Low-voltage electromagnetic actuators for flapping-wing micro aerial vehicles. Sens. Actuators A Phys. 265, 1–9 (2017).
14. C. Y. Wang et al., A sub-100 mg electromagnetically driven insect-inspired flapping-wing micro robot capable of liftoff and control torques modulation. J. Bionic Eng. 17, 1085–1095 (2020).
15. Y. Zou et al., Liftoff of an electromagnetically driven insect-inspired flapping-wing robot. IEEE Trans. Robot. 32, 1285–1289 (2016).
16. N. Hyun, C. M. Chan, A. M. Hernandez et al., Sticking the landing: Insect-inspired strategies for safely landing flapping-wing aerial microrobots. *Sci. Robot*. 10, adq3059 (2025).
17. X. Lu et al., An Insect-Scale Flapping-Wing Micro Aerial Vehicle Inspired by Tumblers Capable of Uncontrolled Self-Stabilizing Flying. *Research* 8 (2025).
18. R. M. Bena et al., High-Performance Six-DOF Flight Control of the Bee++: An Inclined-Stroke-Plane Approach. IEEE Trans. Robot. 39, 1668–1684 (2023).
19. X. Yang et al., Bee+: A 95-mg four-winged insect-scale flying robot driven by twinned unimorph actuators. IEEE Robot. Autom. Lett. 4, 4270–4277 (2019).
20. R. J. Wood, J. P. Whitney et al., Conceptual design of flapping-wing micro air vehicles. Bioinspir. Biomim. 7, 036001 (2012).
21. K. Y. Ma, P. Chirarattananon, R. J. Wood, "Design and fabrication of an insect-scale flying robot for control autonomy" in 2015IEEE/RSJ International Conference on Intelligent Robots and Systems (IROS), (2015).
22. Y. Chen, K. Ma, R. J. Wood, "Influence of wing morphological and inertial parameters on flapping flight performance" in 2016 IEEE/RSJ International Conference on Intelligent Robots and Systems (IROS), (2016).
23. M. Karpelson et al., "Design and fabrication of ultralight high-voltage power circuits for flapping-wing robotic insects" in 2011 IEEE Applied Power Electronics Conference and Exposition (APEC), (2011).
24. E. F. Helbling, R. J. Wood, A Review of propulsion, power, and control architectures for insect-scale flapping-wing vehicles. Appl. Mech. Rev. 70, 010801 (2018).
25. M. Lok et al., "A power electronics unit to drive piezoelectric actuators for flying microrobots" in 2015 IEEE Custom Integrated Circuits Conference (CICC), (2015).

26. B. Goldberg et al., Power and control autonomy for high-speed locomotion with an insect-scale legged robot. IEEE Robot. Autom. Lett. 3, 987–993 (2018).

27. N. T. Jafferis et al., Untethered flight of an insect-sized flapping-wing microscale aerial vehicle. Nature 570, 491–495 (2019).

28. K. Y. Ma et al., Controlled flight of a biologically inspired, insect-scale robot. Science 340, 603–607 (2013).

29. P. Chirarattananon, K. Y. Ma, R. J. Wood, Adaptive control of a millimeter-scale flapping-wing robot. Bioinspir. Biomim. 9, 025003 (2014).

30. N.-S. Park et al., Sticking the landing: Insect-inspired strategies for safely landing flapping-wing aerial microrobots. Sci. Robot. 10, eadq3059 (2025).

31. Z. E. Teoh et al., "A hovering flapping-wing microrobot with altitude control and passive upright stability" in 2012 IEEE/RSJ International Conference on Intelligent Robots and Systems(IROS), (2012).

32. S. B. Fuller et al., Stabilizing air dampers for hovering aerial robotics: Design, insect-scale flight tests, and scaling. Auton. Robots 41, 1555–1573 (2017).

33. J. James et al., "Liftoff of a 190 mg laser-powered aerial vehicle: The lightest wireless robot to fly" in 2018 IEEE International Conference on Robotics and Automation (ICRA), (2018).

34. T. Ozaki, K. Hamaguchi, Bioinspired flapping-wing robot with direct-driven piezoelectric actuation and its takeoff demonstration. IEEE Robot. Autom. Lett. 3, 4217–4224 (2018).

35. T. Ozaki, K. Hamaguchi, Improved lift force of a resonant-driven flapping-wing micro aerial vehicle by suppressing wing–body and wing–wing vibration coupling. Extreme Mech. Lett. 40, 100867 (2020).

36. T. Ozaki, N. Ohta, T. Jimbo, A wireless radiofrequency-powered insect-scale flapping-wing aerial vehicle. Nat. Electron. 4, 845–852 (2021).

37. T. Ozaki et al., Takeoff of a 2.1 g fully untethered tailless flapping-wing micro aerial vehicle with integrated battery. IEEE Robot. Autom. Lett. 8, 3574–3580 (2023).

38. Z. J. Ren, S. Kim, A high-lift micro-aerial-robot powered by low-voltage and long-endurance dielectric elastomer actuators. Adv. Mater. 34, 2270051 (2022).

39. Y. F. Chen et al., Collision resilient insect-scale soft-actuated aerial robots with high agility. IEEE Trans. Robot. 37, 1752–1764 (2021).

40. S. Kim et al., Acrobatics at the insect scale: A durable, precise, and agile micro-aerial robot. Sci. Robot. 10, eabc2897 (2025).

41. Y. H. Hsiao et al., Hybrid locomotion at the insect scale: Combined flying and jumping for enhanced efficiency and versatility. Sci. Adv. 11, eadu4474 (2025).

42. Z. Yao et al., Dynamic doping and interphase stabilization for cobalt-free and high-voltage lithium metal batteries. Nat. Commun. 16, 2791 (2025).

43. C. de Wagter et al., "Autonomous flight of a 20-gram flapping wing MAV with a 4-gram onboard stereo vision system" in 2014 IEEE International Conference on Robotics and Automation (ICRA), (2014), pp. 4982–4987.

44. Z. Liu et al., A wireless controlled robotic insect with ultrafast untethered running speeds. Nat. Commun. 15, 3815 (2024).

45. M. Lok, E. F. Helbling, X. Zhang, R. Wood, D. Brooks, G.-Y. Wei, A low mass power electronics unit to drive piezoelectric actuators for flying microrobots. IEEE Trans. Power Electron 33, 3180–3191 (2017).

46. M. Karpelson, G.-Y. Wei, R. J. Wood, "Milligram-Scale High-Voltage Power Electronics for Piezoelectric Microrobots" in 2009 IEEE International Conference on Robotics and Automation (ICRA), (2009), pp. 2217–2224.

47. M. Karpelson, G.-Y. Wei, R. J. Wood, Driving High Voltage Piezoelectric Actuators in Microrobotic Applications. Sens. Actuators A Phys. 176, 78–89 (2012).

48. M. Karpelson, G.-Y. Wei, R. J. Wood, "A Review of Actuation and Power Electronics Options for Flapping-Wing Robotic Insects" in 2008 IEEE International Conference on Robotics and Automation (ICRA), (2008), pp. 779–786.

49. J. James, S. Fuller, "A High-Voltage Power Electronics Unit for Flying Insect Robots That Can Modulate Wing Thrust" in 2021 IEEE International Conference on Robotics and Automation (ICRA), (2021), pp. 7212–7218.

Methods

Design and Fabrication of the FVW-Fly

The primary structural components of the FVW-Fly include four Y-shaped piezoelectric direct-drive flapping wing modules, a cross-shaped embedded fuselage, and a base. Each Y-shaped piezoelectric direct-drive flapping wing module consists of a piezoelectric actuator and a V-shaped wing (Extended Data Fig.1). The actuators tail end of the four Y-shaped flapping wing modules are inserted into the slots around the fuselage, forming a cross-shaped, omnidirectional flapping-wing aircraft (Fig. 1B). By adopting a forked vibration mechanism for the flapping wings, this design minimizes the vibration-induced power loss and displacement compensation during flight, resulting in a 27.5% increase in the robot's lift over its baseline (Fig. 1D).

The self-stabilization mechanism consists primarily of a damping arm and a damping cylinder. One end of the damping arm is inserted into the central axis slot of the damping cylinder, while the other end is inserted into a circular hole at the top of the cross-shaped embedded fuselage (Extended Data Fig.1). Under aerodynamic damping forces, a three-dimensional restoring torque is generated at the top of the aircraft, imparting self-stabilizing and disturbance-resistant properties to the vehicle during flight.

The piezoelectric actuators, V-shaped wings, and self-stabilizing mechanism are primarily manufactured using the smart composite microstructure (SCM) process, while the cross-shaped embedded fuselage is fabricated using ultraviolet curable 3D printing.

The manufacturing process of the piezoelectric actuator follows a previously established methodology[8]. To facilitate integrated cutting and assembly, all reinforcement structures are made of 125 μm glass fiber. The thickness of the carbon fiber prepreg material is increased from 30 μm to 40 μm to improve the rigidity of the piezoelectric actuator and enhance the adhesive strength of the intermediate bonding layer, thus improving the actuator's lifespan. This modification increases the system's resonance frequency by 7.3%, contributing to the improved lift performance. Both the piezoelectric ceramic plates and the glass fiber contact ends of the actuator are reinforced. The narrower end of the actuator is reinforced with coating and spot gluing techniques (Fig. 1B), while the bottom end is clamped into the fuselage slot and secured with adhesive to increase stiffness at points experiencing higher bending stress, thus extending the robot's lifespan.

The V-shaped wings are fabricated through an integrated folding process. In the previous manufacturing process [17] to facilitate integration, the wing's passive hinge membrane and wing membrane were made from the same thickness of 5 μm polyimide (PI) film. To optimize the aerodynamic characteristics of the wings, the membrane thickness was reduced to 3μm for the wing surface, while the passive hinge membrane thickness was increased to 8μm. During the integrated fabrication, the two types of films were first cut into the designed shapes (Extended Data Fig.1) to facilitate accurate stacking and curing. The V-shaped wings and piezoelectric actuators are assembled into the Y-shaped flapping wing module by aligning the actuator's output end with the positioning grooves on the V-shaped wing's fan-shaped plates (Fig. 1B, Extended Data Fig.1).

The cross-shaped embedded fuselage is fabricated using ultraviolet curable 3D printing (Extended Data Fig.1). The structural material is resin, and four cross-shaped slots are arranged around the fuselage to clamp the flapping wing modules and provide assembly positioning. A through-hole is designed at the top of the fuselage for the installation of the self-stabilization mechanism (Fig. 1B).

The damping arm of the self-stabilization mechanism is made from a 350 μm diameter carbon fiber rod. The damping cylinder is composed of a double layer of 30 μm carbon fiber prepreg and 2 μm Polyethylene terephthalate (PET) film, and is manufactured using the same process described in previous work. First, the carbon fiber prepreg and PET film are laser-patterned and then positioned and stacked using custom-designed molds. The stacked materials are thermally pressed into a composite layer using a flexible negative pressure technique, followed by laser etching to pattern the structure and release it. Finally, the composite material is rolled and formed using a cylindrical mold.

The cross-shaped support frame of the damping cylinder is made of 250 μm carbon fiber rods and a ultraviolet curable 3D printing central axis sleeve. The central axis sleeve is designed with positioning holes in the center and around the perimeter. The carbon fiber rods are inserted into these holes to form the cross-shaped support frame, which is then positioned and fixed at the bottom of the damping cylinder (Extended Data Fig.1).

Self-stability analysis of untethered FVW-Fly system

Due to factors such as manufacturing and assembly imperfections, the structure of FVW-Fly may lack perfect symmetry. This asymmetry can lead to the generation of initial torque during open-loop takeoff, resulting in pitching and rolling of the robot. Furthermore, external disturbances can disrupt the robot's stable flight. To enable the robot to possess self-stability and disturbance resistance, we introduced a cylindrical damper in our previous work [17]. When the robot tilts or shifts, the cylindrical damper experiences aerodynamic drag perpendicular to its surface, generating a restoring torque that helps maintain stability.

The aerodynamic drag is primarily governed by inertial forces, which are influenced mainly by the damper's structure and the relative airflow velocity:

$$F_d = \frac{1}{2} A C_d(\alpha) \rho v^2 \qquad \text{(S1)}$$

where ρ is the air density, C_d is the drag coefficient as a function of the angle of attack α, and A is the area of the damper.

The structure proposed in this paper adopts a full-wing flapping mechanism, enhancing the aerodynamic efficiency. This leads to an increase in the initial unbalanced torque generated, while the system integrates a drive control circuit and a battery module. Using the self-stability framework from prior work, we simplify the state transition matrix for small deviations in the untethered flight system's hovering state:

$$T = \begin{bmatrix} -\frac{k_D + k_r}{m} & -g & \frac{k_D d_D - k_r d_r}{m} \\ 0 & 0 & 1 \\ \frac{k_D d_D - k_r d_r}{I} & 0 & -\frac{k_D d_D^2 + k_r d_r^2}{I} \end{bmatrix} \qquad \text{(S2)}$$

where m is the total mass of the flight system, I is the total moment of inertia after adding the damper, d_D and d_r are the distances from the center of mass of the flight system (COS) to the aerodynamic centers of the damper and wings, and k_D and k_r are the aerodynamic damping coefficients of the damper and wings. We can obtain the characteristic solution for the system, which tends toward stability. However, when the system's oscillation exceeds the robot's inherent stability threshold, self-stable flight is not achieved under practical conditions, demonstrating insufficient self-stability (Extended Data Fig.3B).

Because there is a certain distance between the drive circuit battery module and the flapping wing actuator, we analyze the system's forces by treating the drive circuit, battery module, and wing module separately (Extended Data Fig.3A). Assuming that the flight system experiences an unbalanced disturbance in hovering, causing roll, pitch ($\vec{w}$, $\vec{\theta}$), and lateral displacement ($\vec{a}_c$, $\vec{v}_c$), aerodynamic forces generate corresponding resistances and moments around the damper and robot. The dynamical analysis of the untethered flight system yields the following self-stability control equation:

$$m\vec{a}_c = \sum \vec{F} = \vec{F}_D + \vec{F}_r + \vec{F}_e + \vec{F}_{L,c} \qquad \text{(S3)}$$

$$I\dot{\vec{w}} = \sum \vec{M} = \vec{M}_D + \vec{M}_r + \vec{M}_e + \vec{M}_L \qquad \text{(S4)}$$

$$\begin{bmatrix} \dot{\vec{v}}_c \\ \dot{\vec{\theta}} \\ \dot{\vec{w}} \end{bmatrix} = \begin{bmatrix} -\frac{k_D + k_e + k_r}{m}\vec{v}_c + \frac{k_D d_D - k_e d_e - k_r d_r}{m}\cos\vec{\theta}\vec{w} - g\sin\vec{\theta} \\ \vec{w} \\ \frac{k_D d_D - k_e d_e - k_r d_r}{I}\vec{v}_c - \frac{k_D d_D^2 + k_e d_e^2 + k_r d_r^2}{I}\cos\vec{\theta}\vec{w} \end{bmatrix} \qquad \text{(S5)}$$

where a_c is the acceleration of the lateral movement of the system: $a_c = \dot{v}_c$, $\vec{F}_D$ is the lateral force exerted on the damper by aerodynamic forces: $\vec{F}_D = -k_D\left(\vec{v}_c - d_D\vec{w}\cos\vec{\theta}\right)$, due to the cylindrical symmetry of the damper, the circumferential resistance coefficient *k* remains constant. $\vec{F}_e$ is the lateral force exerted on the drive circuit battery module by aerodynamic forces: $\vec{F}_e = -k_e\left(\vec{v}_c + d_e\vec{w}\cos\vec{\theta}\right)$. $\vec{F}_r$ denotes the lateral force induced by the aerodynamic forces on the robotic wings: $\vec{F}_r = -k_r\left(\vec{v}_c + d_r\vec{w}\cos\vec{\theta}\right)$, $\vec{F}_{L,c}$ refers to the lateral component of the robotic lift force: $\vec{F}_{L,c} = -\vec{F}_L\sin\vec{\theta}$. $\vec{M}_D$, $\vec{M}_e$ and $\vec{M}_r$ represent the torques generated by the forces $\vec{F}_D$, $\vec{F}_e$ and $\vec{F}_r$ on the robotic system $\vec{M}_D = k_D d_D\left(\vec{v}_c - d_D\vec{w}\cos\theta\right)$, $\vec{M}_e = -k_e d_e\left(\vec{v}_c + d_e\vec{w}\cos\theta\right)$, $\vec{M}_r = -k_r d_r\left(\vec{v}_c + d_r\vec{w}\cos\theta\right)$, $\vec{M}_L$ is the torque generated on the system by the robotic lift force, the lift force passes through the center of mass of the robotic system, so $\vec{M}_L = 0$.

The stabilizing effect on the flight system is primarily produced by the restoring torque from the damper. The restoring torque is related to the damping area of the damper and the moment arm. To avoid adding unnecessary weight to the damper, we adjust the length of the torque arm to modify the restoring torque. After changing the length of the damping arm, the system's parameters change accordingly. We fit these parameters as a polynomial function of the damping arm length l and analyze the self-stability performance of the system under different damping arm lengths(Extended Data Table 2, Extended Data Fig.3).

The analysis shows that the flight system's self-stability improves with increasing damping arm length, up to a certain point, beyond which it begins to diminish. This trend is due to an increase in the restoring torque, which initially enhances stability, but excessive torque leads to larger inertial moments, slowing the recovery time, but the system remains stable. The optimal damping arm length for maximum self-stability is 55 mm (Extended Data Fig.3C). Due to inherent asymmetries in the FVW-Fly and initial torque differences of Y-shaped piezoelectric direct-drive flapping wing modules, the actual arm length is slightly longer than 55 mm. In this experiment, a damping arm length of 70 mm was adopted, which, as confirmed by experimental validation, provides better self-stability for the untethered flight system.

Design of half-wave differential sinusoidal high-voltage drive control electronic system

The drive and control electronic system comprises a communication and control module, a sensing module, a boost module, and an inverter module. Fabricated using standard Flexible Printed Circuit (FPC) technology, it adopts a double-layer FPC (Extended Data Fig.4) to reduce circuit area, with dimensions of 9 mm × 10 mm and a total weight of 173 mg (Extended Data Table 2). The HVDCE enables the MCU to receive Bluetooth commands, drive the boost module and inverter module to output high-voltage sinusoidal AC signals, read and process TOF data, and implement closed-loop height control (Fig. 3B). The boost inverter employs a two-stage circuit design. The front stage is a boost-flyback boost circuit: the MCU outputs PWM waves to control MOSFETs for high-frequency switching, thereby converting the low voltage of the lithium-ion battery into a high voltage of 250–300 V. The output voltage amplitude of the booster can be adjusted by controlling the frequency and duty cycle of the PWM. The rear stage is a full-bridge inverter circuit, which realizes inversion by controlling the switching of the H-bridge; only one side of the H-bridge is conducting at any time, enabling alternating driving of the piezoelectric actuator. The electrical model of the dual-crystal piezoelectric actuator can be modeled as a parallel circuit consisting of a capacitor and a series resistor-inductor-capacitor (RLC) circuit. For simplified analysis, this study equates the piezoelectric actuator to a load composed of a parallel capacitor-resistor circuit. Most of the energy of the piezoelectric actuator is stored in the main capacitor, and its driving process can be approximated as the charging and discharging process of the equivalent capacitor. When one side of the piezoelectric actuator is energized while the other is grounded, the end of the piezoelectric actuator generates displacement under voltage excitation—with greater voltage leading to larger displacement. The voltage is gradually increased to the target maximum voltage, at which point the displacement of the piezoelectric actuator reaches its maximum; subsequently, the voltage is gradually reduced to return to the initial position, and the H-bridge is switched. By regulating the switching process of the two sides of the H-bridge, the driving waveform of the piezoelectric actuator can be modulated, enabling the output of a relatively standard sinusoidal waveform.

Power consumption of untethered FVW-Fly system and drive efficiency of HVDCE

The minimum takeoff condition of the FVW-Fly is 210 V/88 Hz, which drives four piezoelectric actuators simultaneously to achieve untethered takeoff. The active power consumption of the four piezoelectric actuators is 160–170 mW. Powered by a DC regulated power supply (Vin = 4.0 V), the total power consumption of the entire HVDCE is approximately 400 mW. Among this, about 10 mW is used for Bluetooth communication and the MCU to drive MOSFETs and transistors, and approximately 20 mW is consumed by the TOF sensor. Thus, the power required by the boost inverter circuit is about 370 mW, leading to an efficiency of approximately 45% for the boost inverter circuit. The energy loss in the circuit is mainly reflected in high-frequency switching loss, as well as losses in the coupled inductor and diodes. The designed high-voltage drive control electronic system is powered by a commercial lithium-ion battery with a capacity of 10 mAh, and the battery's endurance decreases as the output current increases. We tested the battery's endurance under different discharge currents (Fig. 3I), setting the initial open-circuit voltage to 4.2 V and the cutoff discharge voltage to 3 V (the safe cutoff discharge voltage of the lithium-ion battery). After discharge, the voltage will recover to around 3.7 V after a period of rest. The minimum takeoff power consumption of the vehicle is 400 mW, so the minimum required battery discharge current is 100 mA, and the used lithium-ion battery can discharge continuously for 5 minutes (Fig. 3I). However, in the vehicle endurance test, as the battery's operating voltage decreases, it is necessary to dynamically adjust its discharge current to maintain the vehicle's lift. During this process, the maximum discharge current of the lithium-ion battery is approximately 125 mA. The theoretical endurance of the vehicle should exceed 4 minutes and 30 seconds (Fig. 3I), but in actual flight tests, the continuous heating of the boost inverter circuit significantly reduces its energy efficiency, and the sharp rise in the battery temperature greatly shortens its single continuous discharge time. Therefore, the single continuous flight time of the vehicle is 4 minutes, and the vehicle can continue to fly after the power supply system is statically cooled for a period of time. The designed boost inverter achieves high energy efficiency at AC output voltages above 200 V, using fewer components and featuring an ultra-lightweight design, which meets the load capacity constraints of sub-gram flapping-wing micro-aerial vehicles and their requirement for untethered takeoff .

Untethered flight system integration design

The integrated untethered flight system is composed, from top to bottom, of the self-stabilizing mechanism, the cross-shaped four-driver flapping wing module(FVW-Fly), and the lithium battery with the drive control circuit (Fig. 1C and Fig. 3A). The total weight of the integrated cable-free flapping-wing MAV system is 984 mg (Extended Data Table 2).

The drive control circuit is positioned at the bottom of the system, with the boost inverter module facing downward, which includes a TOF sensor. This arrangement facilitates heat dissipation from the transformer module within the circuit, also ensuring proper performance during controlled altitude experiments. Due to the significant weight of the battery and drive control circuitry (523 mg), accounting for more than half of the total system weight (984 mg), it is crucial for system stability that these components be placed as close as possible to the center of gravity of the flight system. Accordingly, the base of the robot is positioned as close as possible to the actuators, with a designed mounting distance of 5 mm. The self-stabilizing mechanism is intended to counteract the pitch and roll torques generated by external disturbances and internal output imbalances during takeoff, ensuring stable flight. To achieve this, the self-stabilizing mechanism is located at the topmost part of the system, and its damping arm length is sufficiently long to overcome the moments of imbalance during flight. Based on the results of the self-stabilization analysis, we adopt a damping arm length of 70 mm.

Altitude feedback control design and calibration

Due to the limited computing power of the MCU and the fact that we only uses the TOF sensor to feedback height data, we only need to adopt a relatively simple PID controller to achieve good height stabilization control, greatly reducing the computing power requirement. The power consumption of the sensor is approximately 20 mW. As the TOF sensor is prone to interference from ambient light during operation, and the voltage amplitude of the HVDCE varies discretely with a regulation interval of 5–10 V, the vehicle will exhibit small-range dynamic floating near the target height when subjected to constant height control. However, such fluctuations are acceptable and do not affect the flight stability of the vehicle. The vehicle we designed can achieve attitude self-stabilizing flight, so it can be assumed that the vehicle is in a vertical state during use. At this time, the motion direction of the micro air vehicle is always opposite to the direction of gravity along the fuselage axis, and its height control dynamics can be expressed as:

$$m\ddot{z} = F_T - c\dot{z} - mg \qquad \text{(S6)}$$

where m is the weight of the micro air vehicle, F_T is the total thrust of the four flapping wings of the micro air vehicle, c is the aerodynamic damping coefficient, and g is the gravitational acceleration.

In this work, the FVW-Fly adopts a TOF sensor for altitude feedback control, which for the first time freed the micro air vehicle from the constraints of the motion capture system. The TOF sensor is based on a 940 nm wavelength VCSEL laser, with a maximum measuring range of 2 m, and data is read via I2C communication. Due to environmental light interference and batch differences, the altitude measurements of the TOF sensor require calibration. The drive and control circuit integrated with the TOF sensor is mounted at the bottom of the micro air vehicle, with the infrared emission port of the TOF sensor facing the ground. Micro air vehicle tests are conducted in the motion capture system to real-time acquire the vehicle's altitude, while the TOF sensor measures at a frequency of 100 Hz and transmits the measured values to the receiving end via Bluetooth. Multiple flight tests are repeated, and the TOF sensor measurement data is compared with the reference altitude obtained from the motion capture system (Extended Data Fig.5A). The sensor measurements exhibit a strong linear relationship with the reference values, with the fitting line expressed as: $y = 1.0187x - 1.089$. This indicates that the altitude sensing system used in this study can accurately capture millimeter-level altitude changes of the micro air vehicle. As can be seen from the figure, the measurement error of the TOF sensor increases with increasing altitude, but within an altitude of 1.5 m, these errors are completely acceptable. The TOF sensor is calibrated using the fitted function, and flight tests are conducted again in the motion capture system. Meanwhile, the reference altitude from the motion capture system and the altitude data measured by the TOF sensor are recorded and plotted (Extended Data Fig.5B). Within 35 seconds, the sensor measurements almost completely coincide with the reference values from the motion capture system, with an average error of 2.6 mm.

Externally Driven Self-Stabilizing Takeoff Tests

To evaluate the self-stabilizing flight capability of the FVW-Fly, self-stabilizing hovering tests were conducted. First, takeoff tests were performed without the self-stabilization mechanism. Test results showed that under fully open-loop conditions (180 V, 88 Hz), affected by manufacturing process errors, airframe coupled torsional oscillation, and cable interference, the robot rolled over and crashed after ascending to a certain height, failing to achieve open-loop stable hovering (Extended Data Fig.6, A and C, movie). Irrecoverable deviations occurred in both the attitude angles and horizontal position of the robot (Extended Data Fig.6D).

Flight tests of the FVW-Fly equipped with the self-stabilization mechanism were carried out under the same fully open-loop conditions (180 V, 88 Hz) (Extended Data Fig.6B, movie S2). After ascending to a certain height, the robot maintained basic stability in the vertical direction with a vertical offset error of less than 4 cm (Extended Data Fig.6C). The horizontal offset distance was within ±18 cm, and the fluctuations in pitch and roll angles were below ±15° (Extended Data Fig.6E). These results demonstrate that the self-stabilization mechanism can significantly enhance the hovering performance of the robot under open-loop conditions.

Open-loop self-stabilizing hovering experiments were conducted at different drive signal amplitudes. The ascending height and takeoff speed of the robot varied with different drive amplitudes, and the takeoff speeds under various drive signal amplitudes were tested separately (Extended Data Fig.7, A to N, movie S3). Using a motion capture system, drive amplitudes ranging from 150 V to 280 V were applied to the aerial vehicle in 10 V increments, and the takeoff time within a 20 cm height was recorded (Extended Data Fig.7O) to calculate the average ascending speed (Fig. 2G). The maximum ascending speed of the robot reached 1.6 m/s at a drive voltage of 280 V, demonstrating excellent flight speed performance.

Three-axis torque control under external drive conditions

Owing to the transverse arrangement of the FVW-Fly's actuators, the distance from the lift force of each flapping wing module to the robot's center exceeds 15 mm, providing a large moment arm that enables the robot to generate enough torque. To verify the torque generation characteristics of the FVW-Fly, the drive signal amplitudes of the four actuators were adjusted to produce varying lift forces, thereby generating pitch, roll, and yaw three-axial torques (movie S8).

To test the three-dimensional torque output characteristics of the FVW-Fly, a six-axis micro-force measurement setup was constructed (Fig. 2D). This setup utilizes a six-axis micro-force sensor as the core force-sensitive unit. The sensor is fixed to a custom base, and the robot is mounted on the sensor via a dedicated fixture to measure the acting forces. With a response frequency of up to 7 kHz and a resolution of 0.1 mN, the sensor's performance indicators, particularly the response frequency, are significantly higher than the operating frequency of the FVW-Fly, fully meeting the test requirements. To accurately characterize the mechanical properties of the robot, a coordinate system (x-y-z axes) was defined: the x-axis is parallel to the actuator axis, the y-axis is perpendicular to the actuator mounting plane, and the z-axis is vertically upward along the lift direction (Fig. 2D).

Pitch and roll moment generation was characterized by mounting the FVW-Fly on a platform capable of dual-axis rotation about the x-axis (pitch) and y-axis (roll). By independently controlling the flapping amplitude and frequency of each Y-shaped flapping wing structure, pitch and roll torques were generated. Periodically varying torques drove the robot to perform two-DOF pitch and roll motions on the fixed platform (Extended Data Fig.2A) at 0.5 Hz. Data captured by a high-speed motion capture system were used to fit the time-dependent curves of the robot's pitch and roll angles (Extended Data Fig.2B) and the motion trajectory of the robot's center (Extended Data Fig.2C). The extreme values of the pitch and roll angles are mainly determined by the limit design of the two-DOF yaw platform, which was set to ±40° in this experiment. Torque tests using the six-axis force measurement setup showed that the vehicle can generate pitch and roll torques exceeding ±0.075 Nmm (Extended Data Fig.2D), which is sufficient to alter the attitude of the untethered FVW-Fly system during flight.

Separate yaw torque generation control was performed on the FVW-Fly. The robot was fixed on a platform rotatable along the z-axis. Yaw torque was generated by independently controlling the flapping stroke speed of each Y-shaped flapping wing structure. Periodically varying torques enabled the vehicle to perform clockwise and counterclockwise yaw rotations on the fixed platform (Extended Data Fig.2E). Data from the high-speed motion capture system were fitted to obtain the time-dependent curve of the robot's yaw angle (Fig.7, F and G). The clockwise yaw speed was lower than the counterclockwise yaw speed, primarily due to the initial yaw torque introduced by the structural asymmetry of the robot. Torque tests demonstrated that the vehicle can generate yaw torques exceeding ±0.01 Nmm (Extended Data Fig.2H), which is sufficient to adjust the yaw attitude of the untethered FVW-Fly system during flight.

Untethered lift-off speed test of the untethered FVW-Fly system

Takeoff speed determines the minimum time for the vehicle to reach the mission site and reflects its maneuverability. To verify the rapid maneuverability of the designed untethered FVW-Fly system, takeoff speed tests were conducted. Different drive signals were applied to the system, and the takeoff time within a 50 cm height was captured to calculate the average ascending speed.

Three drive signals with different amplitudes were set in the experiment: 220 V/88 Hz, 250 V/88 Hz, and 280 V/88 Hz (movie S9). The vehicle ascended at different speeds under the three drive signals, taking 1.04 s, 0.71 s, and 0.49 s to reach 50 cm, respectively (Extended Data Fig.8). The average ascending speeds of the system were 48.4 cm/s, 70.8 cm/s, and 103.1 cm/s, corresponding to the three drive voltages (Extended Data Fig.8D). Notably, the average takeoff speed at 280 V exceeded 1 m/s, making it the fastest among currently available sub-gram untethered FWMAV capable of stable takeoff.

Flight demonstration of untethered FVW-Fly system under high controlled altitude

The designed untethered FVW-Fly system exhibits good altitude-controlled hovering capability. To further verify the wide range and repeatability of its altitude-holding performance, in addition to the height setting experiments of 25cm, 50cm, 75cm, and 100cm, we also conducted height setting experiments of 150cm and 200cm (Extended Data Fig.9, movie S10). After receiving the altitude command via Bluetooth, the flight system rapidly took off to the target altitude, maintained hovering with controllable fluctuations for more than ten seconds, and then descended to the ground upon receiving the landing command. All altitude experiments were performed using a high-speed motion capture system.

For the 150 cm altitude test, the system's position and attitude were tracked (Extended Data Fig.9A), and the tracking data were used to fit the pose variations during hovering. The fitting results showed that the vertical offset error was less than ±10% (Extended Data Fig.9B), the horizontal offset ranged from -25 cm to 35 cm

(Extended Data Fig.9C), and the fluctuations in pitch and roll angles were below ±15° (Extended Data Fig.9D), demonstrating good stability and altitude control performance. For the 200 cm altitude test, a flight process diagram was plotted (Extended Data Fig.9E). Due to the maximum capture height limitation of the high-speed motion capture system, pose data at 200 cm could not be tracked. Nevertheless, the excellent altitude control effect was confirmed by the recorded flight video and the plotted flight process diagram (Extended Data Fig.9E, movie S10).

Repeatable disturbance-rejection self-stabilization flight demonstration

To verify the repeatability of the untethered FVW-Fly system's disturbance rejection capability, multiple hit and pat disturbance experiments were conducted on the system during hovering. Hit disturbance experiments were designed to simulate the effect of small interfering objects disturbing the side of the untethered FVW-Fly system during flight. A wooden stick was used to strike the side of the self-stabilization mechanism of the hovering micro-aerial vehicle. First, the untethered FVW-Fly system was stabilized at 100 cm for several seconds. Then, the side of its self-stabilization mechanism was struck with a wooden stick, causing the flight system to oscillate unstably. After removing the disturbance, the destabilized flight system oscillated for a few seconds and then restored its upright flight attitude under the restoring torque generated by the self-stabilization mechanism, maintaining stable hovering near the set altitude (Extended Data Fig.10A, movie S11). The above disturbance procedure was repeated three times at intervals of several seconds, and the flight system recovered stability after each hit was removed (Extended Data Fig.10A), demonstrating the repeatability of its self-stabilization and recovery capability. Data tracked by the motion capture system were used to fit the spatial position changes (Extended Data Fig.10, B and C) and attitude angle variations (Extended Data Fig.10D) of the system from takeoff to landing during the hit process. The results showed that during the hit disturbance, the system exhibited small vertical fluctuations, horizontal fluctuations exceeding ±25 cm, and pitch/roll angle fluctuations both greater than ±25°. After each disturbance was removed, the system restored stability within 2 s, indicating good repeatability of disturbance rejection performance.

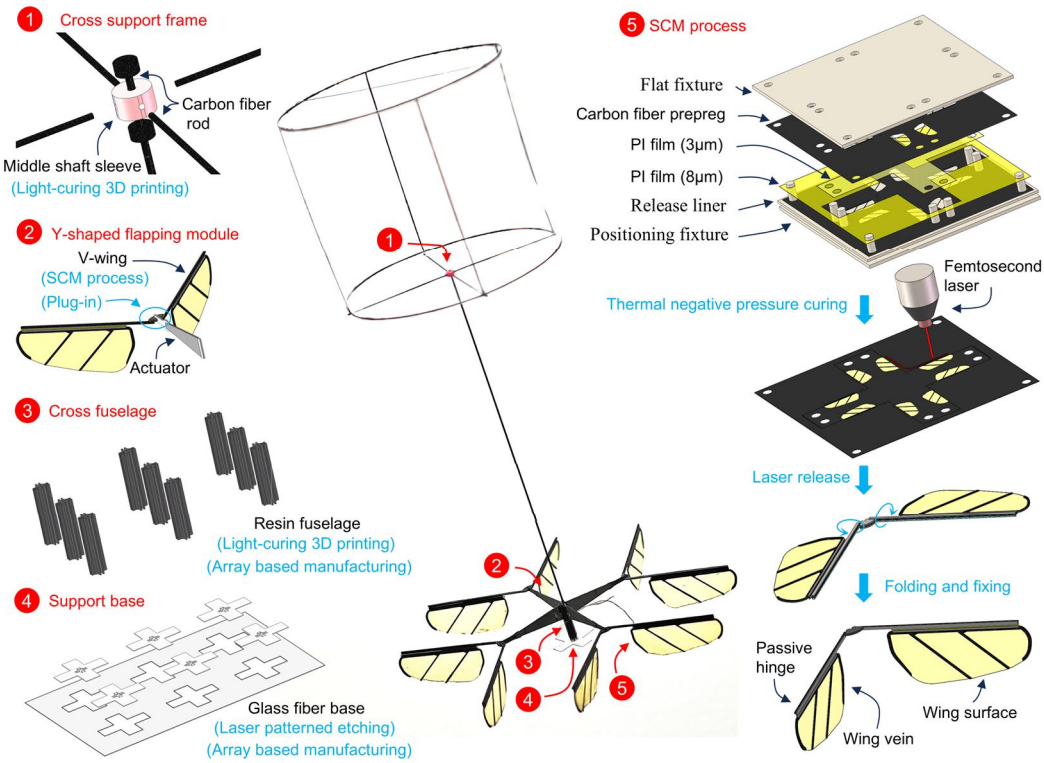
Pat disturbance experiments aimed to simulate the effect of interfering objects disturbing the top of the untethered FVW-Fly system during flight, primarily causing a sudden drop in the flight system's altitude. A wooden stick was used to tap the top of the self-stabilization mechanism of the hovering system. First, the flight system was stabilized at 75 cm for several seconds. Then, the top of its self-stabilization mechanism was patted from top to bottom with a wooden stick, leading to unstable descent. After removing the disturbance, the destabilized and descending system quickly recovered its upright ascending attitude and then stably hovered near the set altitude (Extended Data Fig.10E, movie S12). The above disturbance procedure was repeated twice at intervals of several seconds, and the flight system rapidly recovered and ascended to the hovering state after each pat disturbance was removed (Extended Data Fig.10E), further confirming the repeatability of its self-stabilization and recovery capability. Data tracked by the motion capture system were used to fit the spatial position changes (Extended Data Fig.10, F and G) and attitude angle variations (Extended Data Fig.10H) of the system from takeoff to landing during the pat disturbance process. The results showed that during the pat disturbance, the system exhibited vertical fluctuations exceeding 55 cm, while horizontal fluctuations and pitch/roll angle fluctuations were small. After each disturbance was removed, the system restored stable ascending status within 2.5 s, demonstrating excellent altitude control effect and repeatable disturbance rejection capability in the vertical direction.

Acknowledgments: The authors appreciate the test assistance supplied by the staff of the Microsystem Technology Laboratory, the National University of Defense Technology, and the Hunan MEMS Research Center. This study was supported by the National Natural Science Foundation of China (No:52475039).

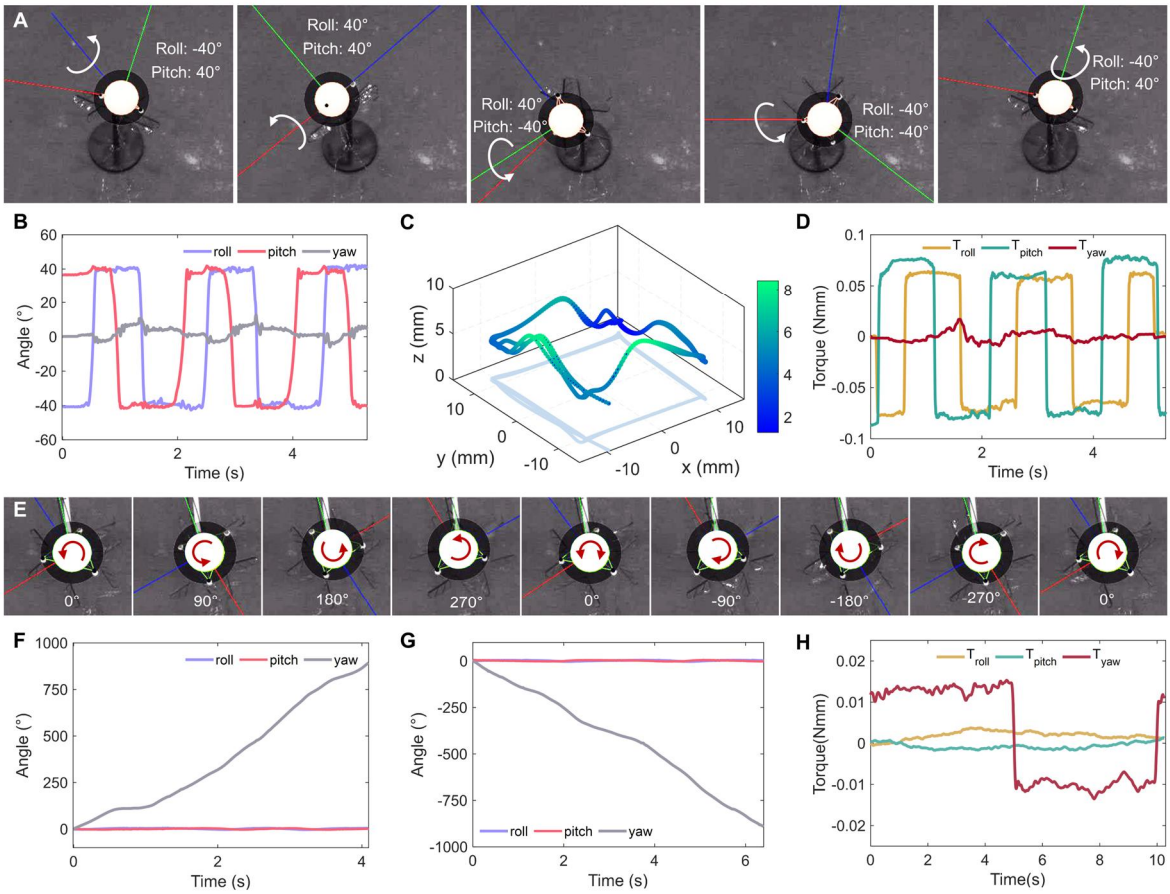
Author contributions: Conceptualization: XL, YW, DX. Methodology: XL, JC, YW. Investigation: XL, JC, ZD, CQ, KL, YC. Visualization: XL, JC, YC, DX. Funding acquisition: YW, XW, DX. Project administration: YW, CY, XW, DX. Supervision: YW, DX. Writing – original draft: XL, JC. Writing – review & editing: XL, YW, JC, YC, CY, ZD, CQ, KL, XW, DX

Competing interests: Authors declare that they have no competing interests.

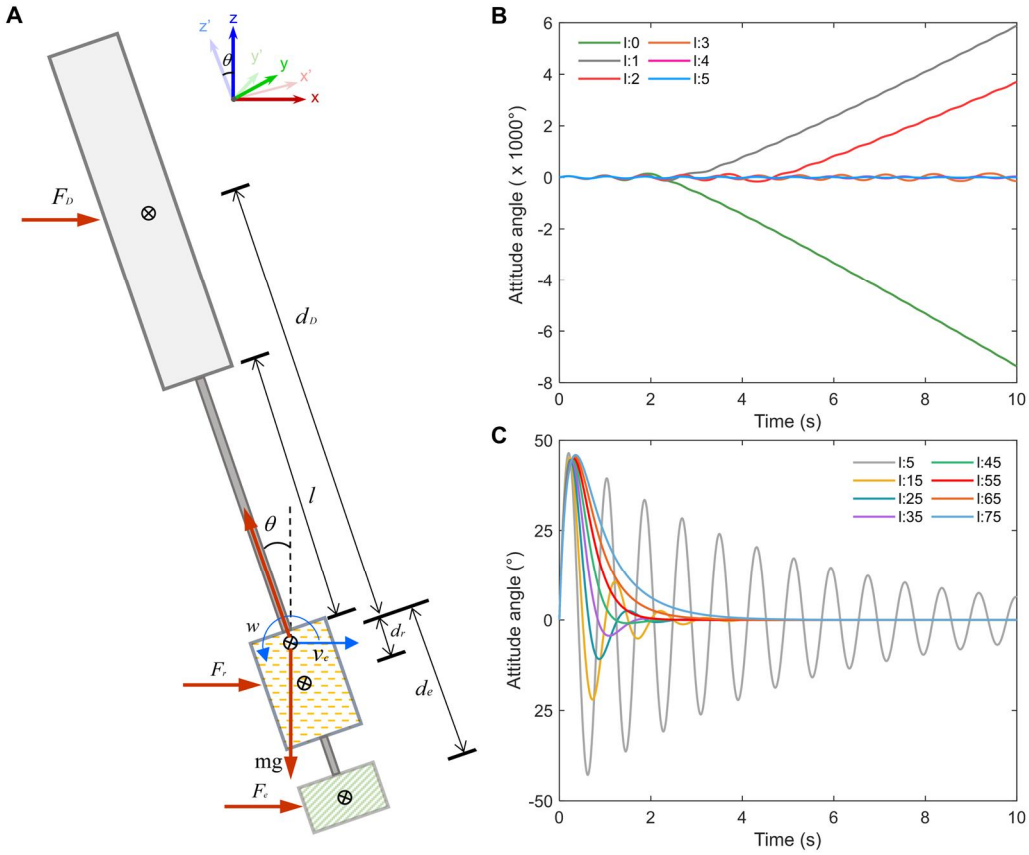
Data and materials availability: All data are available in the main text or the supplementary materials.



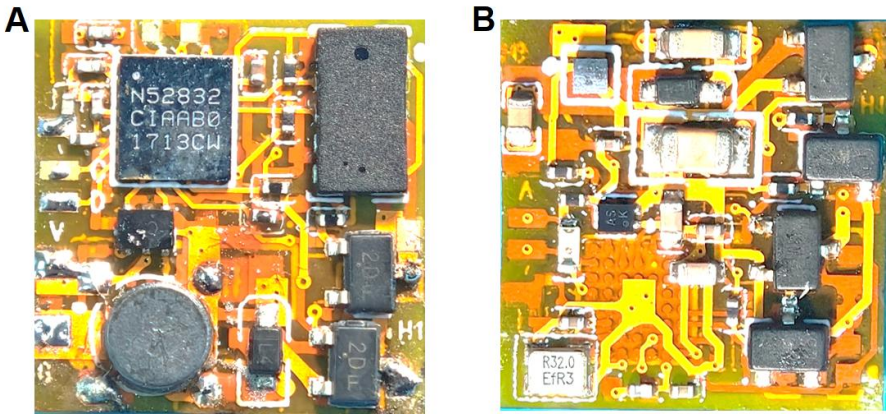
Extended Data Fig.1 Composition and fabrication of the cross four-drive self-stabilizing FWMAV. The robot incorporates a self-stabilizing mechanism, four Y-shaped piezoelectric direct-drive flapping-wing modules, a resin-cross-embedded airframe, and a glass fiber base. Each flapping-wing module consists of a piezoelectric actuator and a V-shaped wing. The manufacturing process of the robot is mainly based on the SCM and ultraviolet curable 3D printing technology.



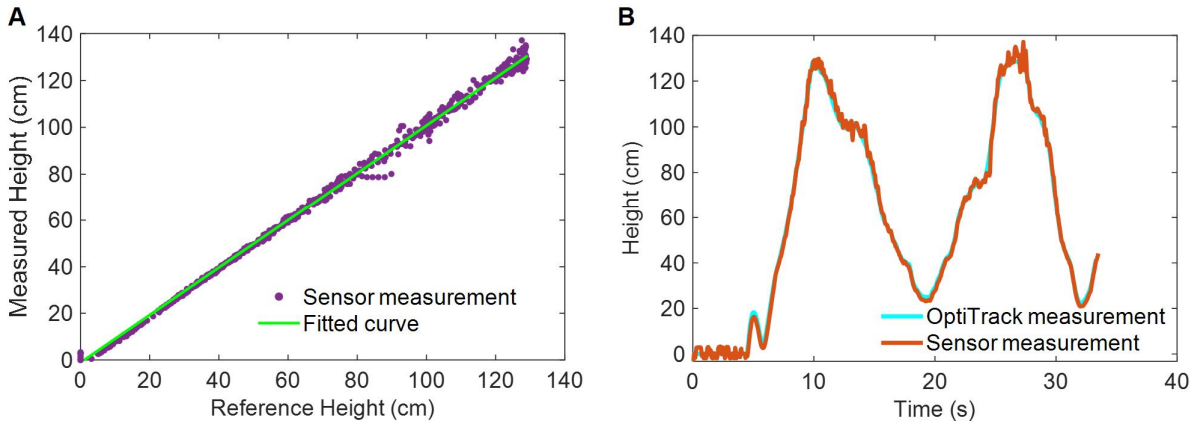
Extended Data Fig.2 Generation of external driving control torques in the cross-four-drive FWMAV. (A) Composite diagram of the deflection motion of the robot's pitch and roll when the two degrees of freedom at the bottom of the fuselage are hinged. **(B)** Corresponding attitude angle variations of the robot in (A). **(C)** Trajectory tracking and fitting curve for the robot's center point in (A). **(D)** Corresponding three-axis torque generation of the robot in (A). **(E)** Schematic of combined clockwise and counterclockwise yaw motions for the robot fixed on a rotary bearing. **(F, G)** Attitude angle variations corresponding to the robot's clockwise and counterclockwise yaw motions in (E), respectively. **(H)** Corresponding three-axis torque generation of the robot in (E).



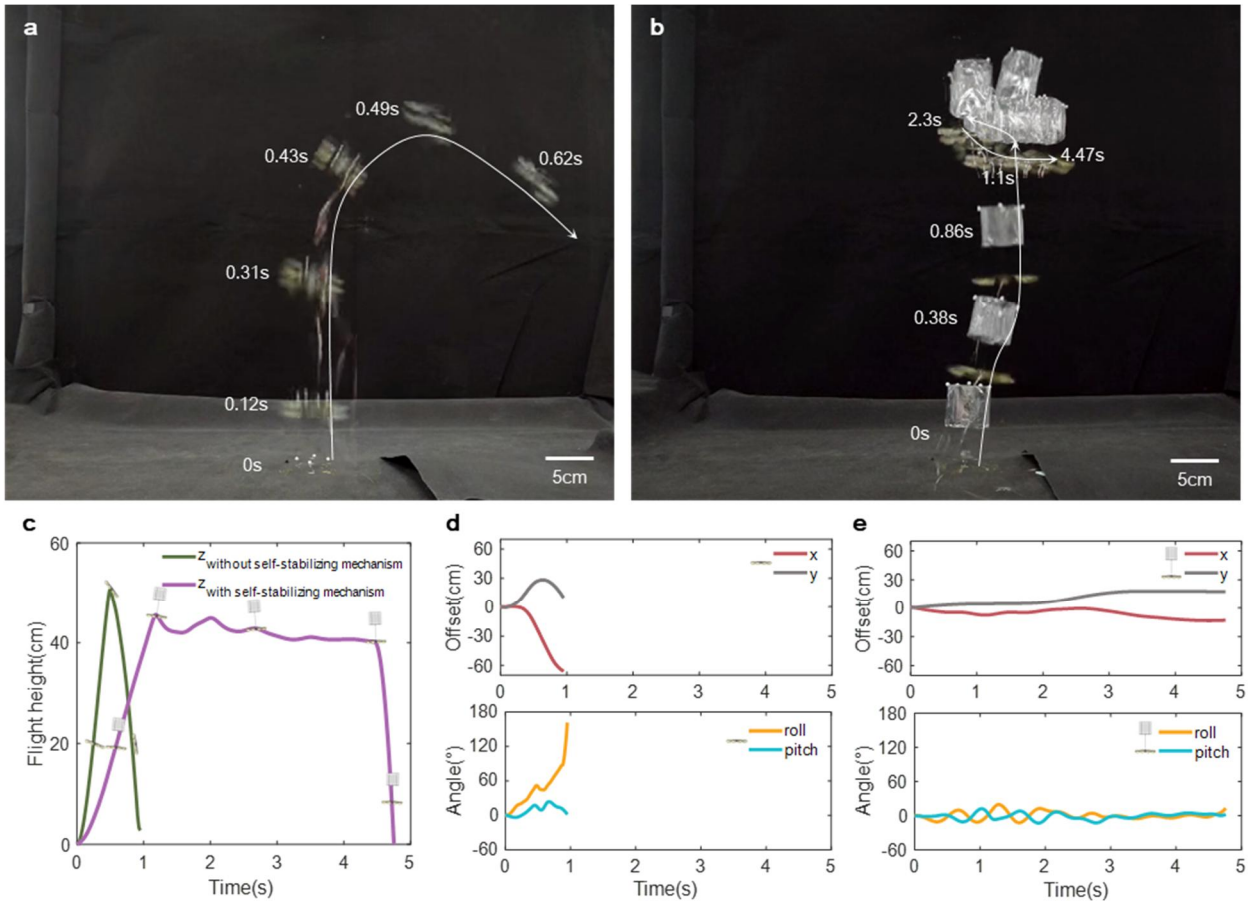
Extended Data Fig.3 Self-Stabilization Analysis of the sub-gram untethered FWMAV system. **(A)** Schematic illustrating the lateral forces and torque model of the robot featuring a cylindrical damper. **(B)** The oscillation and stability recovery process of the untethered robot system under the initial external disturbance with a damper arm length of 0–5 mm. The system fails to stabilize under these conditions. **(C)** The oscillation and stability recovery process of the untethered robot system under the initial external disturbance with a damper arm length of 5–75 mm. Self-stabilization performance initially increases, then decreases with longer damper arms, exhibiting optimal stabilization at an arm length of 55 mm.



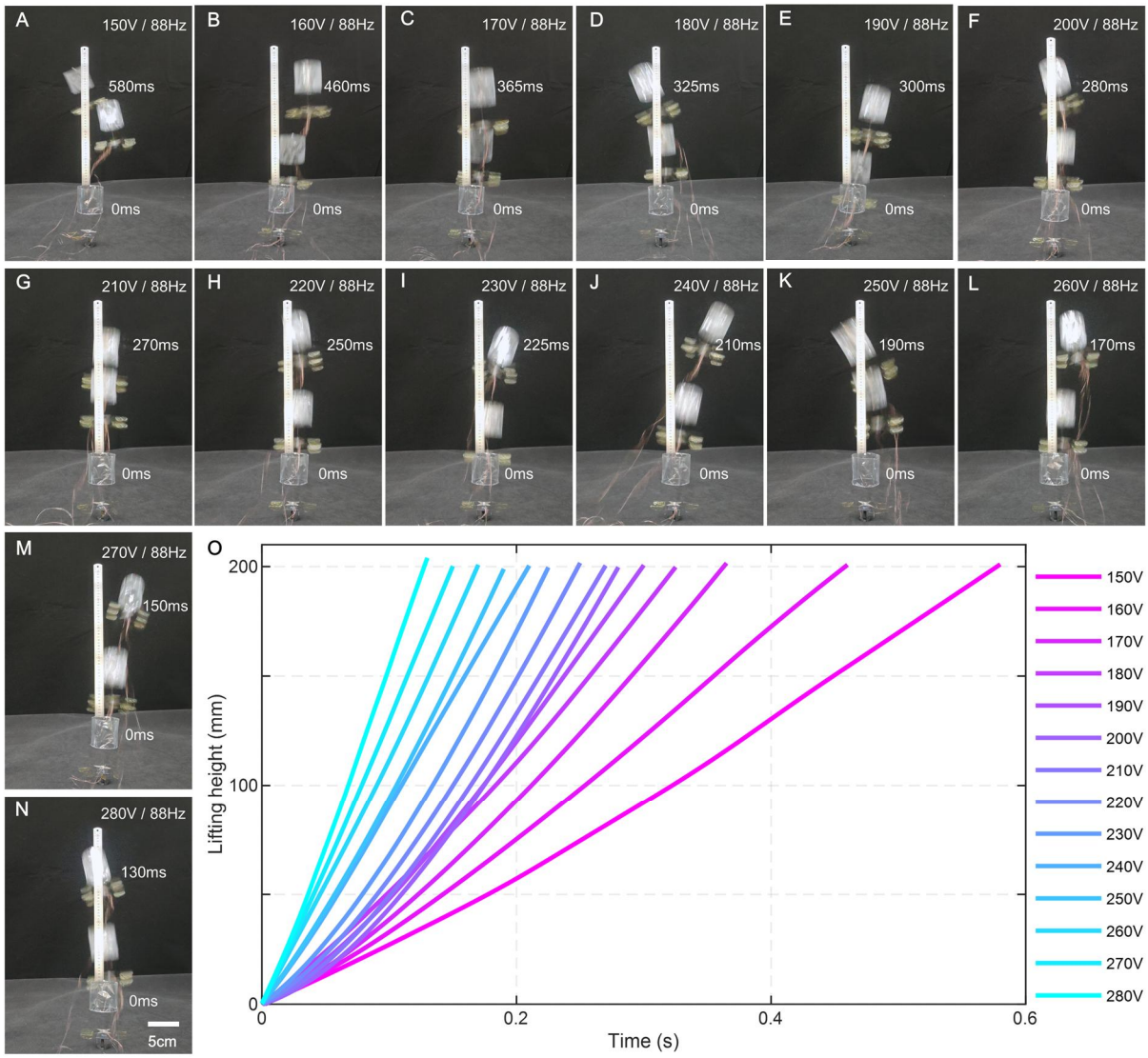
Extended Data Fig.4 Physical diagram of the high-voltage drive control electronic system.(A) Front view of the circuit. **(B)** Photo of the reverse side of the circuit.



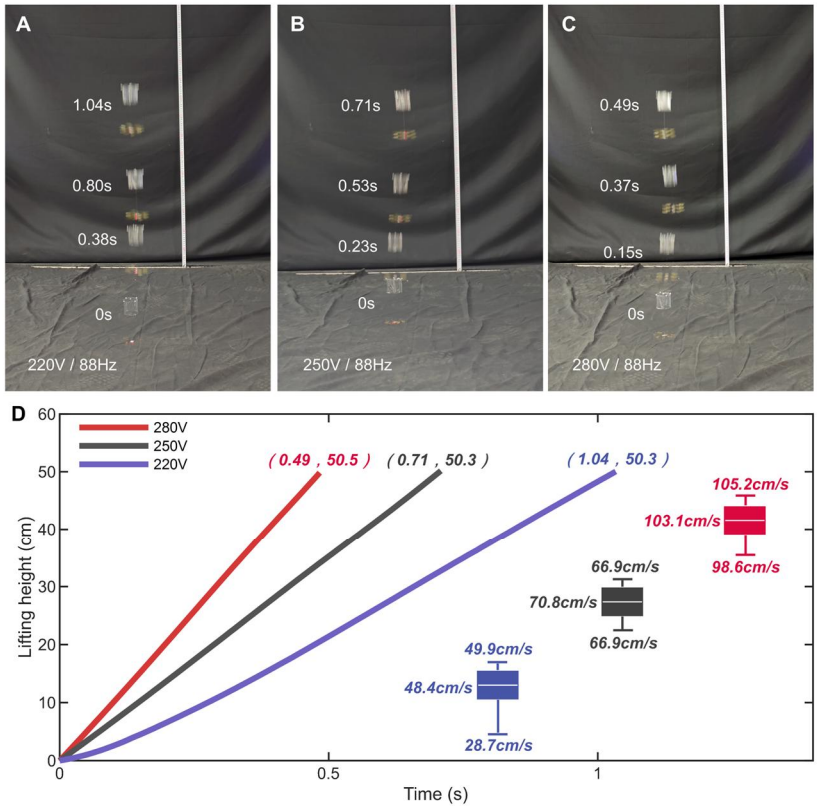
Extended Data Fig.5 Calibration of the TOF sensor. (A) Corresponding relationship and fitting curve between the height measured by the TOF sensor and the motion capture system. As the height increases, the error of the sensor's measured values grows but remains within the allowable range. **(B)** Time-varying curves of the sensor's measured values and the motion capture system's measured values. The sensor data is processed with moving average filtering.



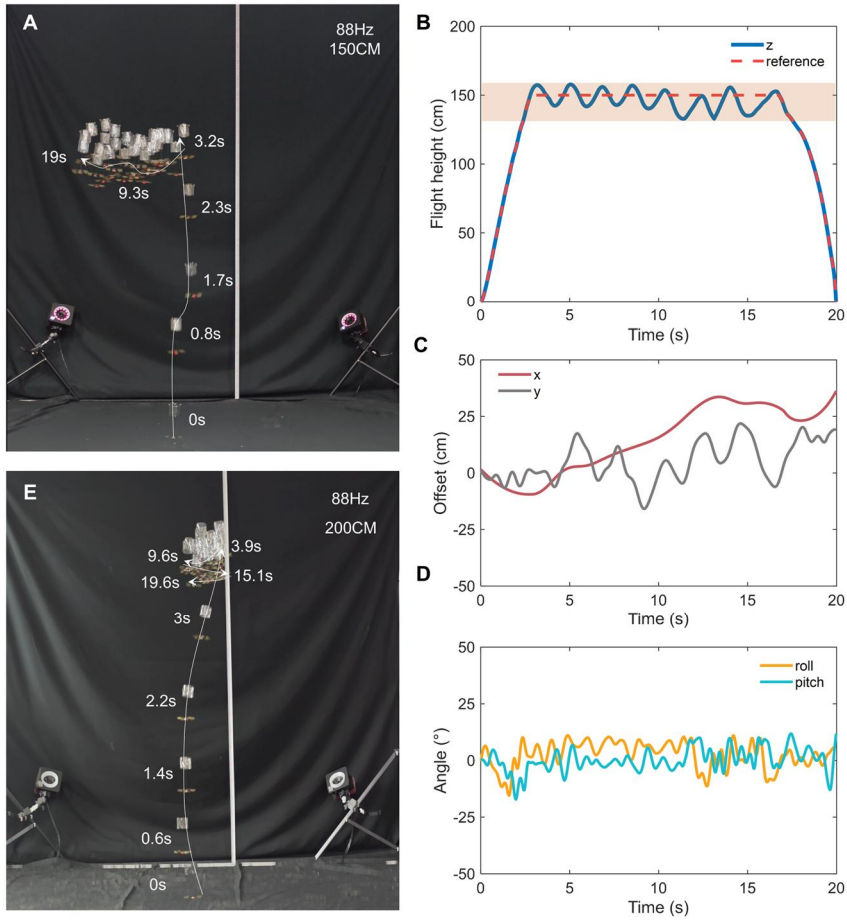
Extended Data Fig.6 Flight performance of the cross-four-drive FWMAV with and without an external self-stabilizing mechanism. (A) The composite image depicts the takeoff process of the robot lacking the self-stabilizing mechanism. The robot toppled over within 1 s after takeoff. **(B)** The composite image depicts the flight process of the robot equipped with the self-stabilizing mechanism. The robot achieved stable hovering in the vertical direction after takeoff. **(C)** Flight altitude versus time curves for robots without (corresponding to A) and with (corresponding to B) the self-stabilizing mechanism. **(D, E)** Horizontal position, pitch angle, and roll angle versus time curves for robots without and with the self-stabilizing mechanism, respectively.



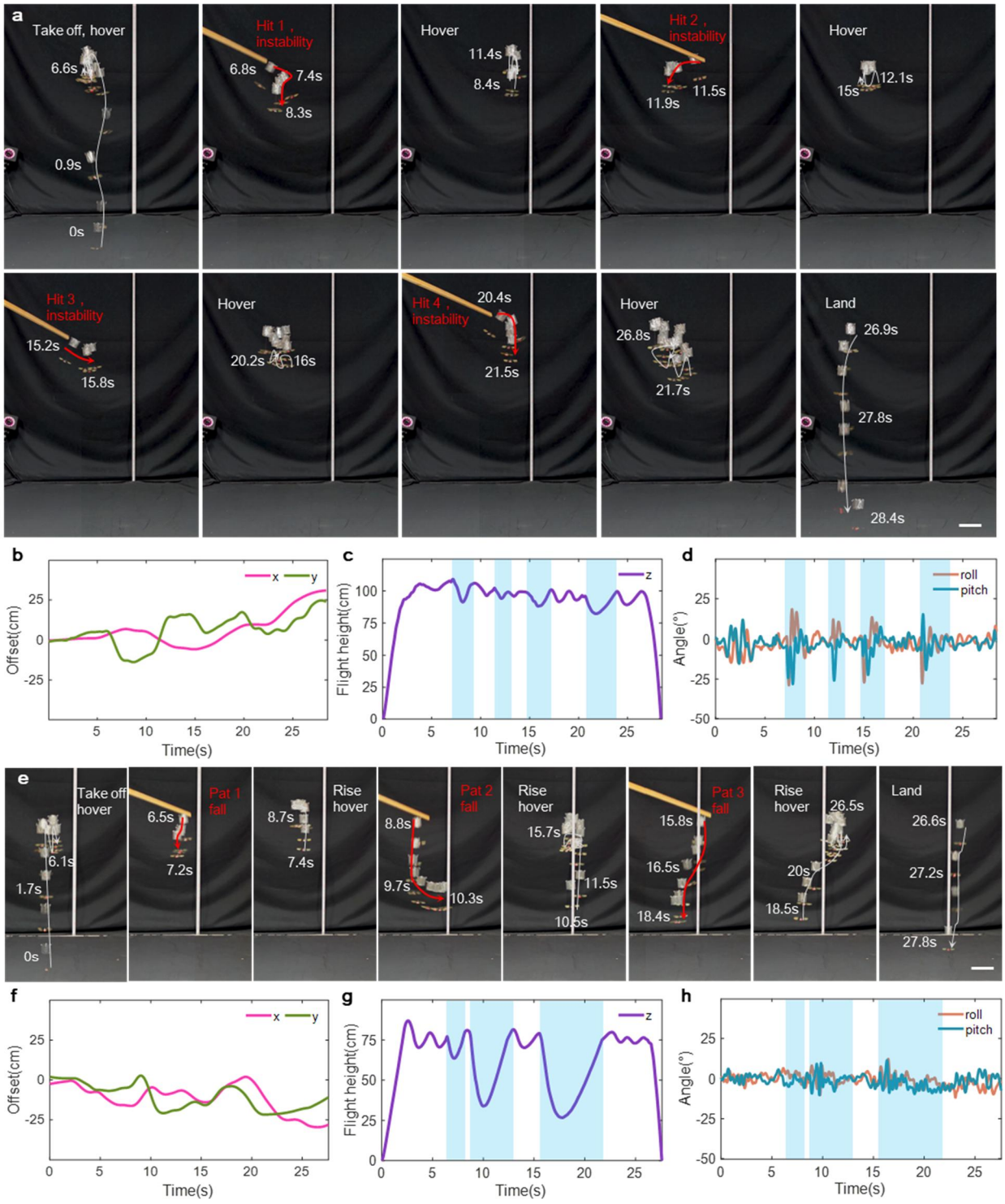
Extended Data Fig.7 Test of the external drive takeoff speed of the cross-four-drive FWMAV. (A-N) Time-lapse composites showing the robot's takeoff process within a 20 cm altitude range at actuation voltages ranging from 160 V to 280 V in 10 V increments. **(O)** Altitude versus time plot for the robot's ascent at actuation voltages from 160 V to 280 V, tracked using a high-speed motion capture system.



Extended Data Fig.8 Untethered lift-off speed test of the sub-gram untethered FWMAV. (A) The untethered system ascended to a height of 50 cm in 1.04 seconds under a 220 V/88 Hz drive signal. **(B)** The untethered system rose to a height of 50 cm in 0.71 seconds under a 250 V/88 Hz drive signal. **(C)** The untethered system rose to a height of 50 cm in 0.49 seconds under a 280 V/88 Hz drive signal. **(D)** Height-versus-time curves for the robot's ascent corresponding to conditions in (A) to (C), tracked using a high-speed motion capture system, the maximum ascending speed of the untethered system is greater than 1m/s.



Extended Data Fig.9 Altitude control performance of the sub-gram untethered FWMAV at higher altitudes. **(A)** Composite image sequence of the robot maintaining altitude-stabilized flight at 150 cm. **(B)** Flight altitude variation during stabilized hover at the 150 cm setpoint. **(C)** Horizontal position drift (XY-plane) during stabilized hover at 150 cm. **(D)** Pitch and roll angle variations during stabilized hover at 150 cm. **(E)** Composite image sequence of altitude-stabilized flight at 200 cm.



Extended Data Fig.10 Repeatable disturbance-rejection self-stabilization flight performance of the sub-gram untethered FWMAV. (A-D) Flight performance under repeated hit disturbances at 100 cm height, composite representation of a flight trajectory resisting multiple impacts (A), position coordinates versus time during hit disturbances (B, C), pitch and roll angles during hit disturbances (D). **(E-H)** Flight performance under repeated patting disturbances at 75 cm height, composite representation of flight trajectory resisting multiple swats (E), Position coordinates versus time during patting disturbances (F and G), Pitch and roll angles during patting disturbances (H).

Extended Data Table 1. The self-stabilizing simulation parameters of the untethered FVW-Fly system, where the variable l is the length of the self-stabilizing mechanism arm.

Symbol	Name	Count / Expression	Units
m	total mass of the untethered system	$0.05 \cdot l + 981$	mg
I	total moment of the untethered system	$60.823 \cdot l^2 + 2302.6 \cdot l + 120960$	$\mathrm{mg \cdot mm^2}$
d_D	damper center to COM	$0.8684 \cdot l - 3 \cdot (10^{-5}) \cdot (l^2) + 20.56$	mm
d_r	flapping wings center to COM	$-1.9399 + 3 \cdot (10^{-5}) l^2 + 0.0635 l$	mm
d_e	circuit and battery center to COM	$3 \cdot (10^{-5}) l^2 + 0.0635 l + 4.4171$	mm
k_D	damper aerodynamic damping coefficient	6.67×10^{-4}	$\mathrm{N \cdot s \cdot m^{-1}}$
k_r	flapping wings aerodynamic damping coefficient	33.94×10^{-4}	$\mathrm{N \cdot s \cdot m^{-1}}$
k_e	circuit and battery aerodynamic damping coefficient	2×10^{-5}	$\mathrm{N \cdot s \cdot m^{-1}}$

Extended Data Table 2. Composition and weight distribution of the untethered FVW-Fly system.

System components		Mass(mg)	Main characteristics
MAVS	Piezoelectric actuator	230	Wingspan: 6.8 Maximum lift: 1.85 g
	V-shaped wings	118	
	Fuselage and base	25	
	Self-stabilizing mechanism	64	
	Glue	16	
	Total weight	453	
HVDCE	Communication and control module	22	Step-up ratio: 86 Maximum output power: 310 mW Efficiency: 45%
	Sensing module	28	
	Boost module	47	
	Inverter module	38	
	FPC substrate and solder	38	
	Total weight	173	
Energy and auxiliary	Lithium-ion battery	350	Capacity: 10 mAh
	Wires and solder	8	
System total weight		984	

Supplementary Files

This is a list of supplementary files associated with this preprint. Click to download.

- MovieS1.mp4
- MovieS2.mp4
- MovieS3.mp4
- movieS4.mp4
- movieS5.mp4
- movieS6.mp4
- movieS7.mp4
- movieS8.mp4
- movieS9.mp4
- movieS10.mp4
- movieS11.mp4
- movieS12.mp4